LRP 403/90 June 1990

Papers contributed to the
17th EPS CONFERENCE ON CONTROLLED FUSION
AND PLASMA HEATING

Amsterdam, The Netherlands, June 1990

INFLUENCE OF AN X-POINT AND ITS POLOIDAL LOCATION ON THE IDEAL MHD STABILITY OF A QUASI-CIRCULAR TOKAMAK.

A.Roy and F.Troyon

Centre de Recherches en Physique des Plasmas
Association Euratom - Confédération Suisse
Ecole Polytechnique Fédérale de Lausanne
21, Av. des Bains, CH-1007 Lausanne/Switzerland

ABSTRACT

The effect of a divertor on the ideal MHD stability of a quasi-circular single-null tokamak is investigated. Five different poloidal positions of the X-point are studied (inside and outside the torus, on the top of the section and two intermediate positions), and compared to an equivalent reference circular case. For low β plasmas, we compute the current limit imposed by the n=1 kink. The stable operating window, in the (q_o,q_{cyl}) plane, is also determined. The lower bound on q_{cyl} is found to be ~1.2 for the divertor configuration. Then the β-limit at different values of the total current is considered. The maximum value of β set by the n=1 mode is comparable for each configuration, except when the X-point points upwards, in which case the maximum is roughly doubled. The results of the ballooning optimization are also presented for the five divertor configurations and for the reference circular case.

1. Introduction.

Experimental results and β optimization studies show that ideal MHD stability imposes a limit on the value of β in tokamaks. Theoretically it was found [1] that the critical β is proportional to the normalized current: $\beta_C=g\, I_N$, with $I_N=\mu_o I(A)/a(m)B(T)$ and $a=(r_{max}-r_{min})/2$, where r_{max} and r_{min} are the maximum and the minimum distance of the plasma surface to the torus axis. Only limiter configurations have been considered. The object of this work is to extend these results to divertor configurations which offer the possibility of reaching a high confinement regime [2].

The most dangerous instabilities are the n=1 free-boundary kink and the ballooning modes, imposing a limit on β, β_k and β_b respectively. The n=1 kink also restricts the total current at low β. The influence of an X-point and its location has already been studied in the case of ballooning modes [3], and Ozeki et al. [4] have computed the axisymmetric stability of divertor configurations for the JT-60 tokamak. They have also investigated the n=1 stability of some cases at low and high β. Our approach is similar to theirs in the sense that the equilibria we are using with ERATO have as plasma boundary, a flux surface just inside the separatrix, but in our study the safety factor at the edge q_S is always kept high (>4-6) and is not a relevant parameter. Only single-null and quasi-circular cross-sections are considered. The angle between the horizontal and the X-point is α_o, $\alpha_o=0$ meaning that it points outward the torus. With $\alpha_o=\pi$ the inverse aspect ratio ϵ is 0.274, ϵ being defined as follows: $\epsilon=(r_{max}-r_{min})/(r_{max}+r_{min})$. The area of the cross-section, normalized to $(R_C)^2=((r_{max}+r_{min})/2)^2$, is always kept constant, and with $\alpha_o=3\pi/4$(fig.1), $\pi/2$, $\pi/4$, 0 the values of ϵ are 0.2261, 0.2124, 0.2261, 0.274. The reference circular case with the same area has ϵ=0.2273. An equilibrium is computed by specifying the pressure gradient $P'(\psi)$ and the surface average current density $J(\psi)$ in two sections:

a) Between the edge and the flux surface where $\psi/\psi_S=a_J$, P' and J are cubic functions of (ψ/ψ_S)

with zero derivative at both ends; $J(\psi=\psi_S)=0$ and $P'(\psi=a_J\,\psi_S)=0$. P' is therefore maximum at $\psi=\psi_S$ (ψ is the poloïdal flux and ψ_S its value at the edge).

b) P'=0 and J constant between $\psi=a_J\,\psi_S$ and the magnetic axis. a_J is determined by the total current I_N and the value of q_0. If $a_J=0$ and q_0 is still too high, the derivative of J on the axis is adjusted.

2. Low β stability.

The operating space at low β has been determined for six configurations: the reference circular case, $\alpha_0=\pi$, $3\pi/4$, $\pi/2$, $\pi/4$ and 0. We are looking for the domain in the (q_0, q_{cyl}) plane, where the equilibria are stable to the n=1 free-boundary kink (q_0 is always larger than 1). The results of the circular case is well-known; the stable window is limited by $q_S>2$, which corresponds here to $q_{cyl}>1.93$. At a given value of q_{cyl}, the highest q_0 is constrained by the fact that one singular surface is necessary and sufficient to have stability. With an X-point the lower limit on q_{cyl} is now about 1.2. At constant current the highest stable q_0 value is always obtained with a J profile having $a_J=0.75$-0.8. The operational diagram obtained with $\alpha_0=3\pi/4$ is shown on fig.2, and with other α_0 the stable domain has the same shape. Table 1 shows the minimum value of q_{cyl} and the corresponding current limit ($q_0\approx1$) for the six configurations considered. The current limit indicated in the last column is computed for B=1.5T and R_C=0.875m. Notice that the divertor configurations can carry a total current about 50% higher than the circular case.

α_0	q_{cyl} min.	I_N max.	I_{phys}(kA) max.
π	1.28	0.880	252
$3\pi/4$	1.26	1.128	267
$\pi/2$	1.19	1.295	287
$\pi/4$	1.25	1.125	266
0	1.24	0.942	270
circ.	1.93	0.737	175

Table1: Current and q_{cyl} limits.

3. β-limit imposed by the n=1 free-boundary kink.

β_k has been computed for the reference circular case and for the divertor configurations. Fig.3 shows the result when $\alpha_0=3\pi/4$, fig.4 when $\alpha_0=\pi/2$ and the six curves of β_k vs. I_N are superposed in fig.5. When $\alpha_0=\pi/2$ (fig.4), β_k is strongly enhanced, reaching a maximum value which is roughly twic that for other positions of the X-point. The g factor ($\beta_k=gI_N$) is larger than that for the reference circular case if $\alpha_0\geq\pi/2$ and lower if $\alpha_0<\pi/2$. For all the divertor cases (except $\alpha_0=\pi/2$), in contrast to the circular cross-section, β_k varies little over a wide range of current.

In order to clarify the dependence of β_k on α_0, additional runs have been made around $\alpha_0=\pi/2$, for a fixed value of the current $I_N=0.84$. The results are on fig.6, where we see that β_k is peaked around $\alpha_0=\pi/2$. In all cross-sections, when β increases, the poloidal field B_p is reinforced outside the torus and weakened inside. For $\alpha_0=\pi$, this increases further the shear in the peripheral region, already large because of the X-point. But for $\alpha_0=0$, this effect reduces the shear at the edge. For $\alpha_0=\pi/2$ there are two poloidal locations where B_p is weak and this seems to be stabilizing.

4. β-limit imposed by ballooning modes.

For a given J profile, β_b is computed by optimizing the pressure gradient on each surface [5]. q_0 is kept around 1 as for the computation of β_k and therefore the second stability regime is not accessible [6]. With $\alpha_0=\pi/2$ (fig.4), β_b is lower than β_k, but for all other configurations (fig.3), including the circular one, β_b is higher. The six curves of β_b are superposed in fig.7. Nothing special at $\alpha_0=\pi/2$ is observed and if $\alpha_0\geq\pi/2$ ($\alpha_0<\pi/2$) the g factor of β_b is higher (lower) than the one of the reference circular case. When α_0 is varied (fig.6) β_k and β_b do not have their maximum at the same

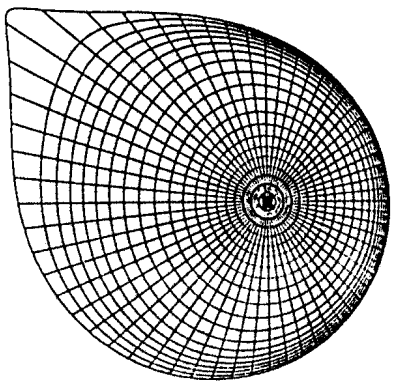

Fig.1: Divertor configuration with $\alpha_o=3\pi/4$.

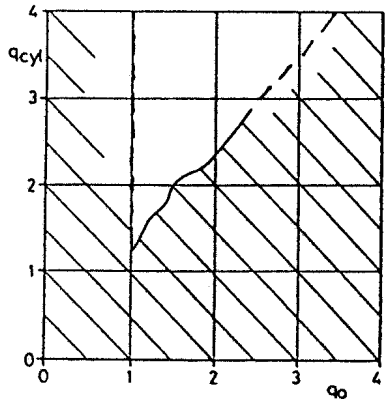

Fig.2: Operational diagram of a divertor configuration with $\alpha_o=3\pi/4$. The dashed region is unstable to the n=1 kink.

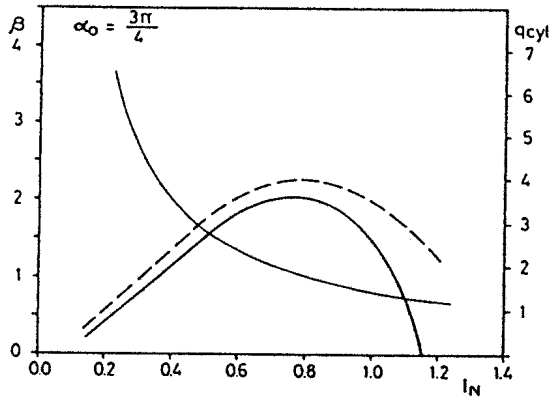

Fig.3: β_k (continuous line), β_b (broken line) and q_{cyl} (thin line) obtained with $\alpha_o=3\pi/4$.

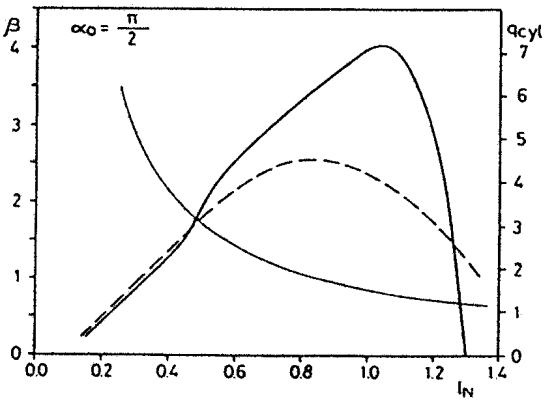

Fig.4: β_k (continuous line), β_b (broken line) and q_{cyl} (thin line) obtained with $\alpha_o=\pi/2$.

Fig.5: β_k obtained with $\alpha_o=\pi$, $3\pi/4$, $\pi/2$, $\pi/4$, 0 and a circular section.

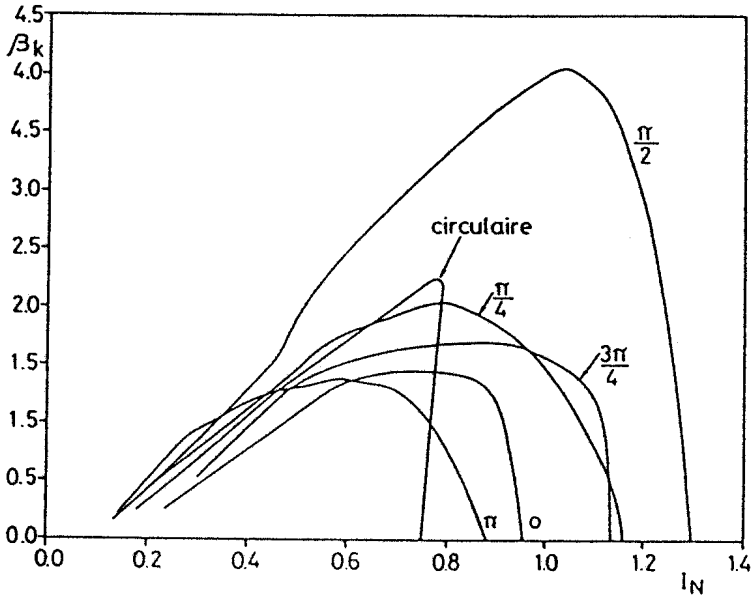

value of α_0. For β_b the maximum is at $\alpha_0=3\pi/8$, where the poloidal extension of the bad curvature region is minimum [5]. Moreover, the X-point is in the bad curvature region for $\alpha_0<3\pi/8$. This may be the explanation of the "strange" position of the maximum of β_b.

5. Conclusion.

Adding an X-point to a quasi-circular cross-section strongly increases the current limit at low β, just as increasing elongation or triangularity. But the β limit does not follow the linear law up to the maximum current. For $\alpha_0=\pi/2$, β_k is enhanced and the β limit is set by ballooning modes. For all other five configurations the kink limit is more constraining and the g factor is larger for $\alpha_0>\pi/2$ than for $\alpha_0<\pi/2$. These results suggest that operation at high β should be possible in a wide range of current. This would favor divertor configurations over limiter ones. We are not aware of experimental results supporting these predictions.

6. References.

[1] F. Troyon et al, Plasma Phys. **26** (1984) 209.

[2] F. Wagner et al., Phys. Rev. Lett. **49** (1982) 1408.

[3] C.M. Bishop, Nucl. Fusion **26** (1986) 1063.

[4] T. Ozeki et al., Nucl. Fusion **28** (1988) 1859.

[5] A. Roy, EPF-Lausanne Thesis (1990).

[6] A. Roy, F. Troyon, in Theory of Fusion Plasmas (Proc. Workshop held at Varenna, Italy, August 1987),Editrice Compositori, Bologna (1988) p143.

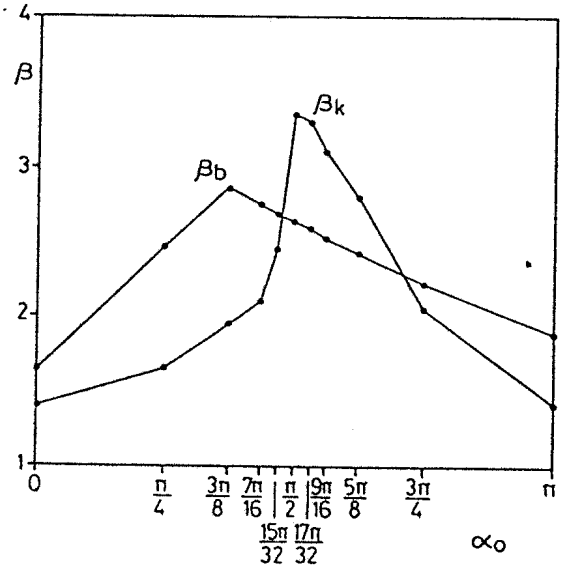

Fig.6: β_k and β_k vs. α_o at I_N=0.84.

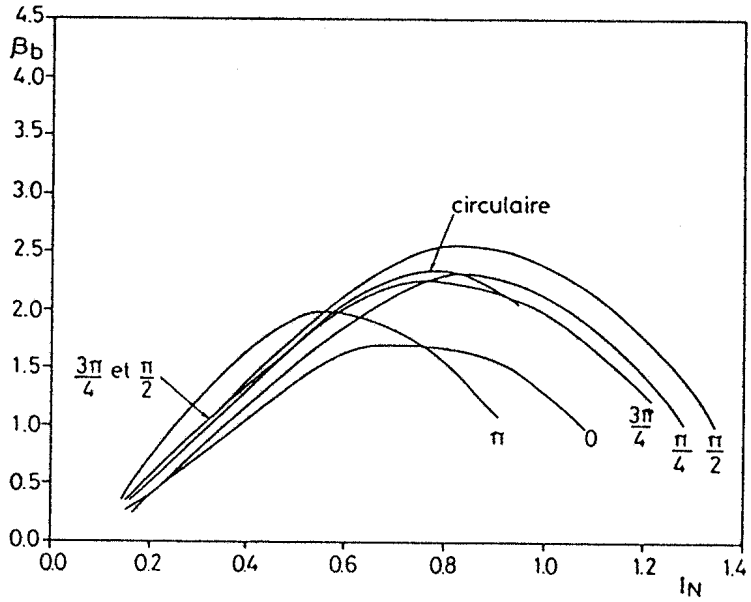

Fig.7: β_b obtained with $\alpha_o=\pi$, $3\pi/4$, $\pi/2$, $\pi/4$, 0 and a circular section.

INFLUENCE OF TRIANGULARITY AND PROFILES ON IDEAL-MHD BETA LIMITS FOR NET

G. Schultz, A. Bondeson, F. Troyon, and A. Roy

Centre de Recherches en Physique des Plasmas
Association Euratom - Confédération Suisse
Ecole Polytechnique Fédérale de Lausanne
Av. des Bains, CH-1007 Lausanne, Switzerland

1. INTRODUCTION Ideal-MHD stability calculations are presented to show the effect of triangularity δ on the beta-limit for plasmas of NET/ITER type with ellipticity $\kappa = 2$ and aspect ratio $A = 3.7$. The optimum betas are achieved as a tradeoff between n=1 ideal kink stability and stability against Mercier and ballooning ($n=\infty$) modes. Two different types of beta-optimisations have been made to study the influence of equilibrium profiles.

In one set of optimisations, the *current* profile is prescribed and the pressure profile is optimised. We impose current profiles that are flat in the central region and decrease monotonically to zero at the edge. For such current profiles, maximum beta is obtained for broad pressure profiles, in particular, for low q_s and small triangularity. The beta-limit is independent of triangularity up to $\delta = 0.4$, but increases slightly for high triangularity, $\delta = 0.6$.

In the other set of optimisations, we specify a more *peaked pressure* profile and optimise the current profile. Peaked pressure profiles, when combined with standard current profiles, for which the central q is flat and near unity, tend to be unstable to localised, pressure driven modes. Therefore, careful tailoring of the central current profile is required. After optimisation of the current profile the n=1 and $n = \infty$ modes give a beta-limit for peaked pressure profiles that is almost unchanged from that for broad profiles, if the cross-section is *sufficiently triangular*, $\delta \geq 0.4$. By contrast, in an *elliptical* cross-section, $\delta = 0.0$, the maximum beta decreases significantly for the peaked profiles.

2. CENTRALLY FLAT CURRENT, OPTIMISED PRESSURE Here we have fixed the profile for the surface averaged toroidal current: it is flat in the central region, zero at the edge, and a cubic polynomial in between with zero derivative at the end points. The pressure profile is optimised. The safety factor at the edge q_s has been varied from 2 to 6.5 and four values of triangularity have been considered: $\delta = 0.0$, 0.2, 0.4, and 0.6. The beta-limit is rather insensitive to q_0 ($1.02 < q_0 < 1.12$) and we give results for only one value, $q_0 = 1.07$. Figure 1 shows β_{max} as a function of the normalised current, I_N.

Figure 1 shows that, for the broad profiles, the beta-limit is almost independent of triangularity for $0 \leq \delta \leq 0.4$, where $\beta_{max} \approx 4.6$ %. A certain gain results from increasing δ to 0.6, which gives $\beta_{max} \approx 5.6$%. However, triangularity has a stronger effect on the maximum normalised current $I_N = \mu_0 I/aB_0$, which increases from about 2.35 at $\delta = 0$ to about 3 at $\delta = 0.6$. As a consequence, $g = \beta_{max}/I_N$ decreases with triangularity. With q_0 held fixed at 1.07, the beta-limit is usually set by ballooning/Mercier modes, except for large triangularity and high current $q_s < 3$, where the limit is set by the n = 1 kink mode.

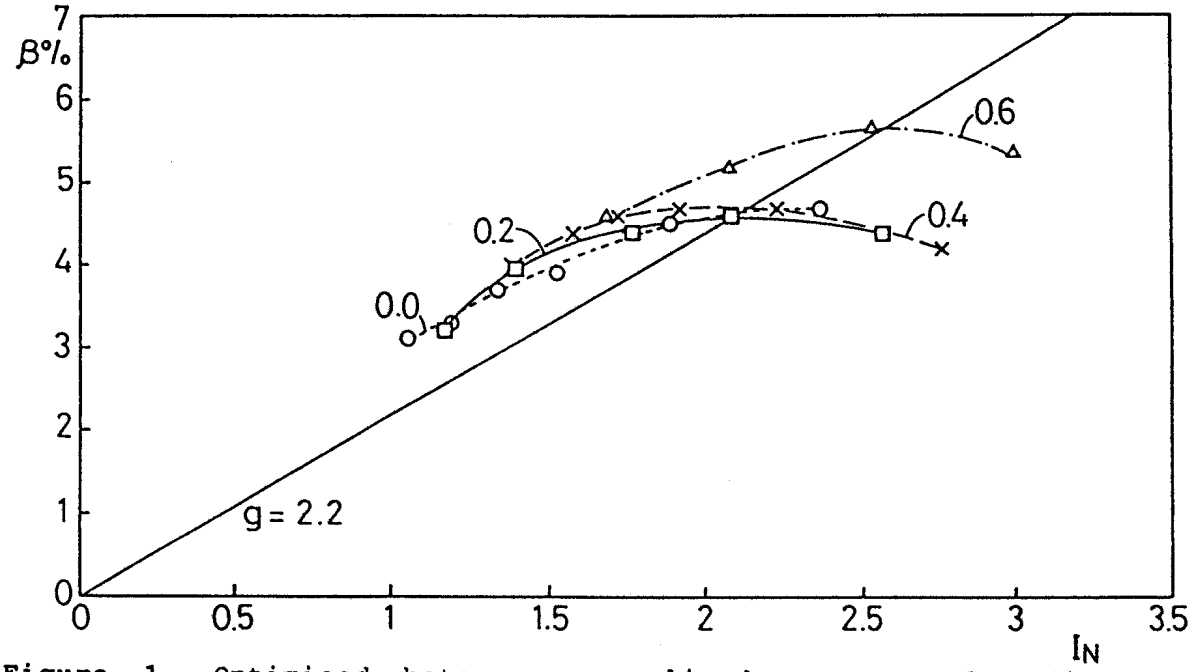

Figure 1. Optimised beta vs normalised current, for different triangularities. The straight line shown is $g = \beta/I_N = 2.2$.

β_{max} does not degrade significantly for $q_s < 3$. Such degradation as well as the so-called ravines in β_{max} for q_s just below integer values have been reported in other studies[2], in which $\langle J_\phi \rangle$ was not kept sufficiently small at the edge. With our choice for $\langle J_\phi \rangle$ which goes quadratically to zero at the edge, such ravines do not occur.

3. PEAKED PRESSURE PROFILES Pressure profiles observed in most tokamaks are more peaked than those found to give the highest beta in ideal-MHD stability studies. Therefore, we have studied the beta-limit for a prescribed peaked pressure profile where dp/dr ≈ constant for $|r-R| > 0.1a$. (r is the major radius in the mid-plane z=0, and R is the major radius of the magnetic axis.)

To test the sensitivity of the results to the choice of current profile, we have applied two different classes of current profiles with the peaked pressure profile, corresponding to two different strategies for improving Mercier stability in the central region. The first class of profiles have a rounded step in the current density near the centre and, outside this step, a monotonically decaying $\langle J_\phi \rangle$ to increase the shear. The second class has a reduced central current density or, equivalently, an increased q_0. For both these types of current profiles, the cases with $\delta \geq 0.4$ give beta-limits for $n = 1$ and $n = \infty$ stability close to those for the broad pressure profile. For small triangularity, $\delta = 0.2$, and even more so for $\delta = 0.0$, the beta-limit for strongly peaked pressure is substantially lower than for the broad profiles.

Figure 2 shows the beta-limits for strongly peaked pressure, obtained with the high-shear current profile and q_0 held fixed at 1.02. For high triangularity, there are relatively minor differences from the results obtained for the broad profiles. Notably, β_{max} for $\delta = 0.6$ drops slightly from 5.6 % to 5.1 %, while for $\delta = 0.4$, the peaked pressure plus optimised current profile even improves the maximum beta from about 4.6% to 5.2 %. Figure 2 shows that beta as a function of current is almost the

same for $\delta = 0.4$ and $\delta = 0.6$. The two curves in Fig. (2) show broad maxima of $\beta_{max} \approx 5.1$ % at $I_N \approx 2.2$, where q_s is about 3.1 and 3.7, respectively. For lower triangularities $\delta = 0.0$ and 0.2 the beta-limit with peaked pressure profiles (Fig. 2) is clearly lower than for the broad profiles (Fig. 1).

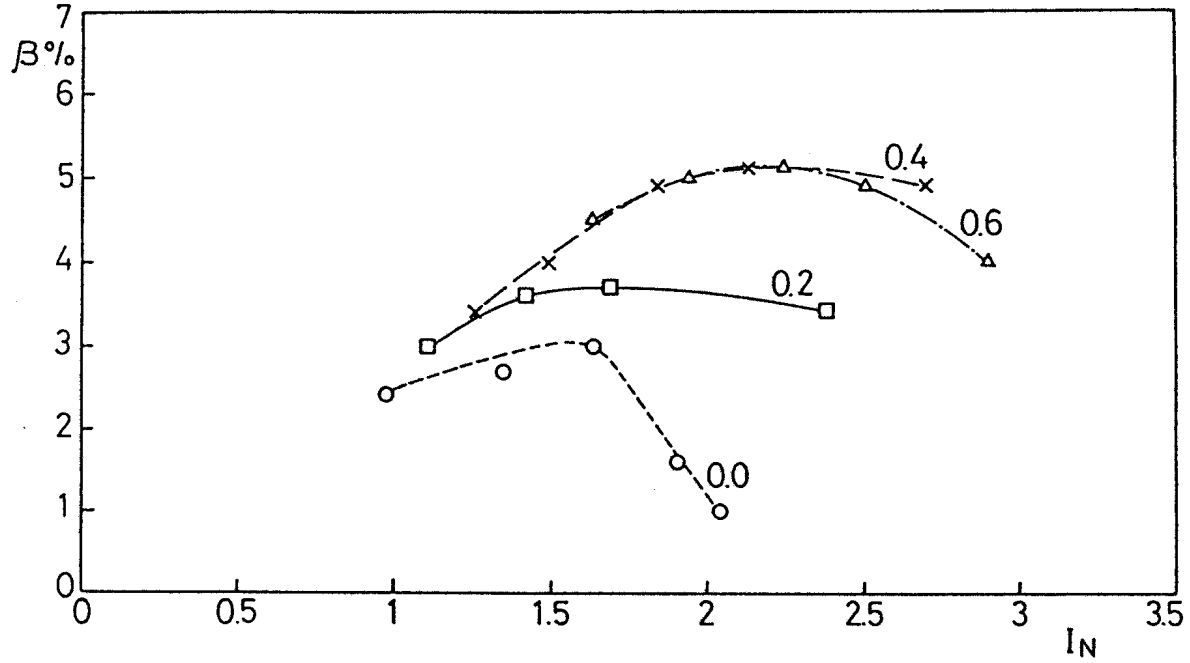

Figure 2. Optimised beta vs normalised current for different triangularities. A peaked pressure profile is prescribed and the current profile has been optimised, using a central step .

To indicate what current profiles are required to give sufficient central shear for a strongly peaked pressure profile and $q_0 = 1.02$, we show in Fig. 3 optimised equilibria with (a) $\delta = 0.6$, $q_s = 3.65$ and (b) $\delta = 0.0$, $q_s = 3.31$. The height of the step is about 10 % for the triangular

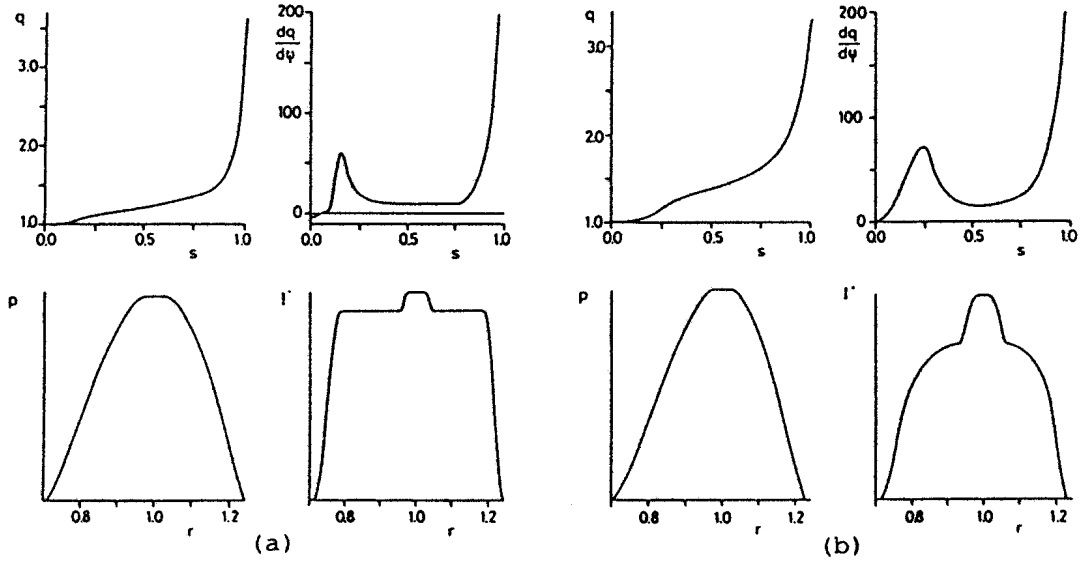

Figure 3. Equilibria with strongly peaked pressure profile and optimised, high-shear current profile. In (a) $\delta = 0.6$, $q_s = 3.65$, $\beta = 5.2\%$, $\beta^* = 6.5\%$, $\beta_0 = 14.7\%$, and $l_i = 0.58$. In (b) $\delta = 0.0$, $q_s = 3.31$, $\beta = 2.9\%$, $\beta^* = 3.6\%$, $\beta_0 = 8.0\%$, and $l_i = 0.72$.

equilibrium and 30 % for the ellipse. As expected, triangularity reduces the amount of shear needed for Mercier stability in the centre. The optimal height of the step increases with q_s.

Stability to n =1 and n = ∞ modes can also be achieved, even for a centrally flat current distribution, by increasing q_0. The resulting beta-limit for high triangularity δ = 0.4 and 0.6 is very similar to that of the high-shear current profile (Fig. 2). For small triangularity, δ = 0.2 and 0.0, the limit is inferior to that in Fig. 2. For the optimised equilibria with raised q_0, q_0 increases with q_s and decreases with triangularity from 1.02 at q_s = 2.0 for δ = 0.6, to 1.57 at q_s = 6.5 for δ = 0.0. The highest beta is reached for δ = 0.4, where β = 5.4%, β^* = 6.8%, and β_0 = 15.0%.

An important difference between the high-shear equilibria and those with a raised q_0 lies in the stability to intermediate-n modes. We have made spot checks of the n = 2, 3, and 4 stability of the two sets of equilibria with peaked pressure profile, optimised for n =1 and n = ∞ stability. We find that, whereas the the high-shear profiles are generally stable, the low-shear profiles with a raised q_0 tend to be unstable to the so-called infernal modes[3]. However, it appears that the beta-limit set by infernal modes for these profiles is only slightly lower than the n = 1, n = ∞ limit.

In summary, optimisations with prescribed, *peaked* pressure profiles show clearly advantageous effects of triangularity, and for $\delta \geq 0.4$, high beta can still be confined by an optimised current profile. For the strongly peaked pressure profile, we find a maximum beta of about 5.1 % both for δ = 0.4 and δ = 0.6, with β^* = 6.4 % and a central beta β_0 = 14.5 %. For the ellipse, these values are considerably lower, β_{max}= 3.0%, β^*= 3.7% and β_0= 8.3%.

4. CONCLUSION The main conclusions of the present study are easy to formulate. For *broad* pressure profiles, triangularity has little effect on the beta-limit. For *peaked* pressure profiles, triangularity has a clear positive effect, and $\delta \geq 0.4$ is highly favourable. To confine strongly peaked pressure profiles with high beta, the q-profile must have sufficient shear in the central region for local stability. The necessary central current gradients decrease with increasing triangularity. The current profiles for highly triangular cross-sections with $q_0 \geq 1$ and low q_s are considerably flatter than those maintained at steady-state in ohmic discharges, and will require non-inductive current drive.

ACKNOWLEDGEMENT This work was supported by NET under contract 310/88-7 FU CH NET and by the Swiss National Science Foundation.

REFERENCES

[1] TROYON, F., GRUBER, R., SAURENMANN, H., SEMENZATO, S., SUCCI, S., Plasma Phys. Controlled Fusion **26** (1984) 209.

[2] PHILLIPS, M.W., TODD, A.M.M., HUGHES, M.H., MANICKAM, J., JOHNSON, J.L., PARKER, R.R., Nucl. Fusion, **28** (1988) 1499.

[3] MANICKAM, J., POMPHREY, N., TODD, A.M.M., Nucl. Fusion **27** (1987) 1461

GLOBAL IDEAL MHD STABILITY OF 3D PLASMAS WITH PSEUDO-VACUUM TREATMENT FOR FREE-BOUNDARY MODES

U. SCHWENN, D.V. ANDERSON*, W.A. COOPER**, R. GRUBER**, S. MERAZZI**
Max-Planck-Institut für Plasmaphysik
IPP-EURATOM Association, D-8046 Garching
**NERSC Livermore, USA*
***EPFL Lausanne, Switzerland*

The determination of the ideal MHD stability properties of plasma containment devices is never complete without the investigation of the impact that can be had by the class of instability that can displace the plasma-vacuum interface. These free-boundary modes impose in many cases the severest restrictions on the plasma beta that a configuration can achieve and/or the toroidal plasma current that can flow within it. In order to examine the free-boundary stability of a plasma, the potential energy contribution of the vacuum region that surrounds the plasma must be added to the internal contribution of the plasma itself. In two-dimensional (2D) plasmas, two methods have been developed to tackle the vacuum contribution to the energy principle. One scheme uses a Green's function technique which is particularly convenient when the conducting wall is placed at infinity. An alternative scheme is to treat the vacuum region as a pressureless and shearless pseudo-plasma. The main advantage of this scheme is that the structure of the problem in the vacuum region is identical to that in the plasma region. A detailed analysis and comparison of the two methods in 2D axisymmetric and helically symmetric geometry has been discussed by Gruber and Rappaz (1985) /1/ and by Gruber et al. (1981)/2/.

We have generalized the vacuum treatment as a pseudo-plasma to three dimensional (3D) geometry and implemented it in the TERPSICHORE ideal MHD stability code, which was previously limited only to the study of internal structures /3/. For this purpose, we identify (s, θ, ϕ) as the Boozer magnetic flux coordinate system within the plasma domain and introduce the coordinate system (s_v, θ_v, ϕ_v) in the vacuum domain subject to the constraints that $s_v = s = 1$, $\theta_v = \theta$ and $\phi_v = \phi$ at the plasma-vacuum interface. Furthermore, we introduce a pseudo-magnetic field $\mathbf{T}$ that satisfies $\nabla \cdot \mathbf{T} = \mathbf{T} \cdot \nabla s_v = 0$, which in most general form can be written as

$$\mathbf{T} = \frac{\mathrm{d}\Phi_v}{\mathrm{d}s_v}\left[\left(\frac{\mathrm{d}\Psi_v}{\mathrm{d}\Phi_v} - \frac{\partial\lambda_v}{\partial\phi_v}\right)\nabla\phi_v \times \nabla s_v + (1 + \frac{\partial\lambda_v}{\partial\theta_v})\nabla s_v \times \nabla\theta_v\right] .$$

Invoking as a gauge condition that the perturbed magnetic field vector potential $\mathbf{A}$ have no components aligned with $\mathbf{T}$, we can introduce a pseudo-displacement vector ξ_v that we express in a form that is quite similar to that in the plasma such that $\mathbf{A} = \xi_v \times \mathbf{T}$.

$$\xi_v = \sqrt{g_v}\frac{\Phi'(1)X_v}{(\mathrm{d}\Phi_v/\mathrm{d}s_v)}\nabla\theta_v \times \nabla\phi_v + \frac{\mathbf{T} \times \nabla s_v}{T^2}Y_v ,$$

The vacuum energy thus becomes

$$\delta W_{\rm v} = \frac{1}{2} \int_1^{s_{\rm vmax}} {\rm d}s \int_0^{2\pi/L_s} {\rm d}\phi_{\rm v} \int_0^{2\pi} {\rm d}\theta_{\rm v} \sqrt{g_{\rm v}} \, [\nabla \times (\boldsymbol{\xi}_{\rm v} \times \mathbf{T})]^2$$

where L_s is the number of periods of the instability structure in one toroidal transit and $s_{\rm vmax}$ is the value of $s_{\rm v}$ at the conducting wall.

The boundary condition at the plasma-vacuum interface $\nabla s \times \mathbf{A} = -(\boldsymbol{\xi} \cdot \nabla s)\mathbf{B}$ reduces to $(\boldsymbol{\xi}_{\rm v} \cdot \nabla s)\mathbf{T} = (\boldsymbol{\xi} \cdot \nabla s)\mathbf{B}$, where $\mathbf{B}$ is the equilibrium magnetic field and $\boldsymbol{\xi}$ is the perturbed displacement vector from the plasma side, from which we obtain

$$\frac{{\rm d}\Psi_{\rm v}}{{\rm d}\Phi_{\rm v}} = \frac{\Psi'(1)}{\Phi'(1)}$$
$$\lambda_{\rm v}(1, \theta_{\rm v}, \phi_{\rm v}) = 0 \text{ and}$$
$$X_{\rm v}(1, \theta_{\rm v}, \phi_{\rm v}) = \xi^s(1, \theta, \phi)$$

where $\xi^s \equiv \boldsymbol{\xi} \cdot \nabla s$. To avoid introducing fictitious resonances in the vacuum region, we impose that ${\rm d}\Psi_{\rm v}/{\rm d}\Phi_{\rm v} = \Psi'(1)/\Phi'(1)$ everywhere. Furthermore, for simplicity, it is convenient also to choose $\lambda_{\rm v}(s_{\rm v}, \theta_{\rm v}, \phi_{\rm v}) = 0$. The boundary condition at a conducting wall $\nabla s_{\rm v} \times \mathbf{A} = 0$ reduces to $X_{\rm v}(s_{\rm vmax}, \theta_{\rm v}, \phi_{\rm v}) = 0$.

To construct the geometry of the vacuum region in order to apply a pseudo-plasma treatment, we have developed a procedure that guarantees that the Jacobian and the metric elements, and thus the geometry, vary smoothly across the plasma-vacuum interface into the vacuum region. Within this procedure, the shape of the conducting wall can be arbitrarily prescribed or is dictated by the shape of the plasma-vacuum interface subject to the conditions that the radial derivatives of R, the distance from the major axis, of v, the geometric toroidal angle, and of Z, the distance from the horizontal midplane, be constant throughout the vacuum domain. In either case, the shape of the conducting wall does not coincide in general with that of the plasma-vacuum interface, and therefore the approach we have followed differs from that in the ERATO code. Two important constraints are imposed in the development of the vacuum region. These are that the vacuum pseudo-surfaces remain always nested and that the conducting wall should not intersect the major axis. The nestedness constraint precludes, in general, that a prescribed conducting wall can approach the plasma-vacuum interface too closely. The alternative scheme for describing a conducting wall, however, will not violate the nestedness constraint even for a wall arbitrarily close to the plasma-vacuum interface.

The vacuum energy acquires a structure that is similar to that obtained from the internal plasma energy with a Fourier decomposition of the perturbations like that undertaken in the plasma. The bulk of the computational effort in the vacuum region concentrates on the calculation of 6 double Fourier flux tube integrals. As the integrals involved here are of the same type as those evaluated inside the plasma, the very efficient MULFI technique can be applied which transforms the discretized integrations into MXM operations /4/.

Applying finite hybrid elements for the radial discretisation of the vacuum energy, we recover the special block pentadiagnonal structure of the matrix equation that was a feature of the formulation of the internal plasma problem in the TERPSICHORE code. Thus, the internal plasma potential energy principle can be straightforwardly combined with the vacuum potential energy principle so that the ideal MHD stability to global modes can be evaluated in a single step. Furthermore, the efficient computational tools previously developed to solve for the eigenvalues of the system in the fixed-boundary problem are applied to the free-boundary problem with virtually no additional effort.

The pressureless and shearless pseudo-plasma treatment of the vacuum region that we have described has been implemented in the TERPSICHORE code. Benchmark studies of analytic Solove'v equilibria have been carried out and compared with results obtained with ERATO /5/. Because the right-hand side matrix in TERPSICHORE is basically the unity matrix rather than derived from the physical kinetic energy as in ERATO, a direct comparison of the magnitude of the eigenvalues is not possible except at points of marginal stability. In Solove'v equilibria, the most unstable free-boundary mode computed by both codes never crosses a marginal point, remaining always unstable. The second most unstable mode, which closely tracks the most unstable fixed-boundary mode, is shown in both codes to become critical when the q-value at the magnetic axis approaches 0.59 for $n = 2$ instabilities in a case with a circular aspect ratio of 3.

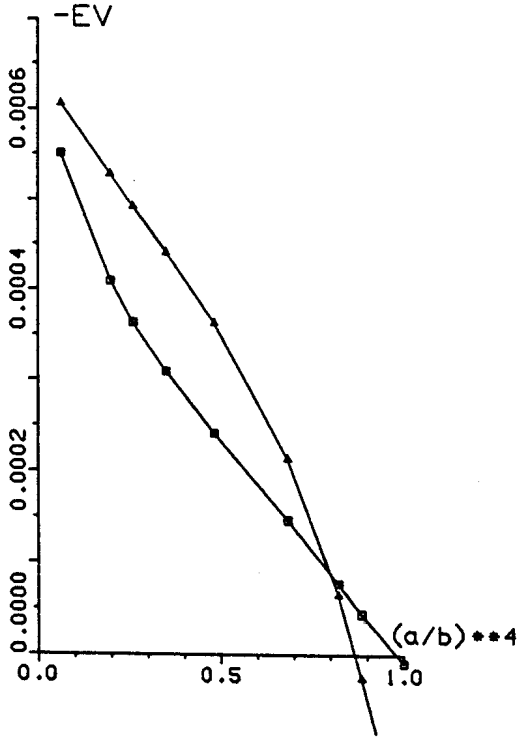

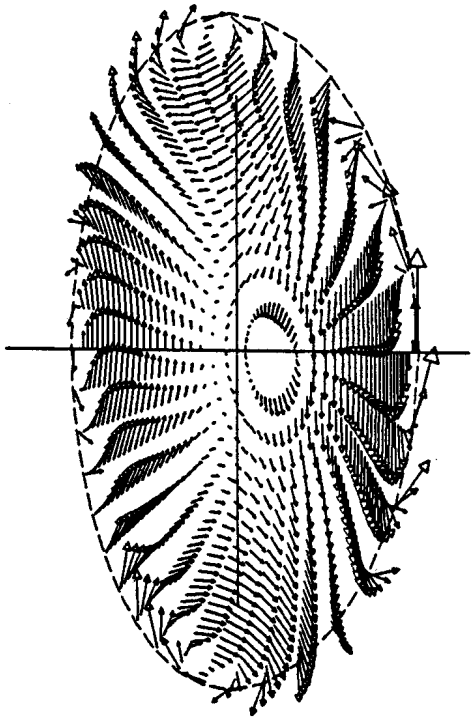

Fig. 1: (left) Eigenvalues as functions of (a/b) for $n = 1$ ($\square$), $n = 2$ ($\triangle$) free-boundary modes in an $\ell = 2$ stellarator with $A = 10$, $\iota = 0.43 \ldots 0.49$ and $\beta_0 = 1.9\%$.

Fig. 2: (right) Eigenfunction of an $n = 1$, $m = 2$ free-boundary mode, data as in Fig. 1, $b/a = 6$, 24 radial, 36 poloidal and 12 toroidal intervals.

A real 3D test was performed by reproducing former results obtained with the STEP code for toroidal $\ell = 2$ stellarators /6/. We chose an $A = 10$ configuration where ι varies from 0.43 to 0.49, a parabolic pressure profile with $\beta_0 = 1.9\%$, and five periods on the torus. This configuration proved to be stable to internal resonant modes due to the finite toroidal aspect ratio. Displacing the conducting wall away from the plasma-vacuum interface led to unstable external modes resonant with $m_{\text{res}} = 2n$. The equilibrium for the TERPSICHORE input was produced with the most recent VMEC code in the fixed-boundary mode /7/. Figure 1 shows the dependence of the eigenvalues for $n = 1$ and $n = 2$ modes on the fourth power of the ratio between the mean radii of the conducting wall b and of the plasma-vacuum interface a. The marginal points found with STEP could easily be reproduced with an accuracy mostly determined by the completely different equilibrium input. Figure 2 shows a typical displacement pattern for an $n = 1$, $m = 2$ mode. As in the former TERPSICHORE results for fixed-boundary global modes, extrapolation studies proved to be mostly unnecessary.

In summary, we have described a method to evaluate free-boundary ideal MHD instabilities in 3D equilibria with nested flux surfaces which has been successfully implemented in the TERPSICHORE code and tested against the results obtained with ERATO for Solove'v equilibria and with STEP for toroidal $\ell = 2$ stellarator equilibria.

REFERENCES

1. R. Gruber, J. Rappaz, Finite Element Methods in Linear Ideal MHD (Springer Verlag, Heidelberg 1985).
2. R. Gruber, S. Semenzato, F. Troyon, T. Tsunematsu, W. Kerner, P. Merkel, W. Schneider, Comput. Phys. Commun.**24** (1981) 363.
3. D.V. Anderson, W.A. Cooper, R. Gruber, U. Schwenn, Theory of Fusion Plasmas (Bologna, 1989) 93.
4. D.V. Anderson, W.A. Cooper, R. Gruber, S. Merazzi, U. Schwenn, International Journal for Supercomputer Applications 1990 (to be published).
5. D. Berger, L.C. Bernard, R. Gruber, F. Troyon, ZAMP **31** (1980) 113.
6. F. Herrnegger, Proc. Workshop on Wendelstein VII-X , Schloss Ringberg 1987, EUR 11058 EN (1987) 49.
7. S.P. Hirshman, J. Nührenberg, U. Schwenn, J. of Comput. Phys.**87** (1990) (to be published).
   O. Betancourt, S.P. Hirshman, private communication.

SIMULATION OF MHD ACTIVITY DURING DENSITY LIMIT DISRUPTIONS IN JET

R. Parker, A. Bondeson, and M. Hugon*

Centre de Recherches en Physique des Plasmas, Ass. Euratom - Confédération Suisse
Ecole Polytechnique Fédérale de Lausanne
21 Av. des Bains, CH-1007 Lausanne, Switzerland

*) JET Joint Undertaking, Abingdon, Oxfordshire, United Kingdom

1. INTRODUCTION

The operation of tokamaks is limited to densities below some threshold value which, in ohmic discharges, is proportional to the plasma current. When the density limit is exceeded, the discharge usually disrupts, because the profile contracts and becomes MHD unstable when the radiation losses equal, or exceed, the input power [1,2]. (However, recent experiments performed with beryllium coating or boronisation have shown non-disruptive behaviour at the density limit.) Here, we report on a simulation study of density limit disruptions, in which radiation losses were specified according to experimental data from a disruption in JET [2]. The MHD activity was simulated by a reduced-MHD code with a simple transport model [3]. The simulations reproduce the sequence of events observed during density limit disruptions in JET, starting with m=3/n=1 activity, followed by strong growth of the m=2/n=1 mode, a sequence of minor disruptions, and finally a major disruption, in which the current profile flattens over almost the entire plasma, leading to a large drop in internal inductance, and an accompanying negative voltage spike.

It is well known that the m=2/n=1 resistive tearing mode plays a key role in the disruption process, and this is recognised by existing mode-coupling [4] and quasi-linear [5] models of disruptions, and is also very clearly seen in our simulations. However, the simulations presented here give a scenario, different from that of previous theories [4,5], for the final phase of the disruption, including the so far ill-understood phase where the current profile broadens. In our simulations, the major disruption occurs in two steps, in agreement with observations on JET [2]. First, a large fraction of the central temperature is lost in an "energy quench", which occurs as a sawtooth modified by the large amplitude 2/1 mode. At the end of the energy quench, the magnetic field in the central $q \approx 1$ region becomes stochastic because of the simultaneous presence of modes with different helicities, notably 2/1, 1/1, and 3/2. In a major disruption, good flux surfaces are never restored again, the kinetic energy of several modes continues to grow, and in the final phase, the activity is dominated by the 2/1 and a rapidly growing 3/1 mode.

2. NUMERICAL MODEL

The basic model adopted here is three-dimensional resistive reduced MHD including anisotropic heat conduction, with $\chi_\perp << \chi_{||}$ [3]. The model of Ref. [3] has been upgraded by including radiation losses in the temperature evolution equation. These losses are introduced as a front moving inward from the edge of the plasma. The amplitude, width, and position of the front are prescribed as functions of time in accordance with measurements on JET [2]. Moreover, we use neoclassical resistivity [6], which gives rise to rather peaked current profiles that are strongly Δ'-stable in the absence of radiation losses. The resistivity is taken as a function of the temperature, and our model thus includes the thermal instability discussed in Ref. [7]. To make nonlinear simulation possible, it is necessary to reduce the Lundquist

number S from the very high values in JET (close to 10^9). To accomplish this, we multiply all dissipative terms (such as $\chi_\perp$, resistivity η and viscosity ν) by the same factor E, and shorten the time-scale for variation of the prescribed radiation by the same factor.

3. TIME HISTORY OF ONE RUN

In Fig. 1, we show the time-evolution during one entire run of (a) electron temperature in the centre, r=0.54a and r=0.75a, (b) internal inductance l_i and loop voltage V_l, and (c) the m=2/n=1, m=3/n=2, and m=3/n=1 components of the radial magnetic field at the wall. The enhancement factor E was 2000 in this run, 16 different m/n Fourier components were used and the radial resolution was 150 grid points. The profile for $\chi_\perp$ was adjusted to give a steady-state temperature profile (without radiation) in agreement with that of JET shot #11051, and was then kept fixed in time, and the radiation losses were prescribed according to the same shot. The radiation is turned on at time t=0, but no mode activity is observed in the simulation until $t=2000\tau_A$. At this time the radiation front has reached $q \approx 3$, and the m=3/n=1 resistive tearing mode reaches sufficient amplitude to be visible in the B_r signal (Fig. 1c). With the radiation time-scale sped up by a factor E=2000, the m=3 mode does not have time to saturate before the radiation front has moved inside the q=3 surface. It should be noted that the m=3 mode is stable, or at most marginal from a Δ' analysis, but the resistivity perturbations destabilize a mode that is partly "rippling". As the current profile contracts further, and the radiation front approaches the q=2 surface, the m=2/n=1 mode becomes unstable at $t=2900\tau_A$. There follows a phase of several minor disruptions, during which the B_r signal at the wall reaches about 14 G. The minor disruptions are triggered by increases in the 2/1 amplitude, and disturbances leading to field stochasticity propagate inward from the q=2 surface. During each minor disruption a sawtooth-like relaxation occurs in the $q \approx 1$ region. The standard m=1/n=1 sawtooth mode is modified by the large amplitude 2/1 perturbation and involves large components m=3/n=2 and m=1/n=0, all coupled by the m=2/n=1.

4. THE MAJOR DISRUPTION

As seen from Fig. 1b, the internal inductance first rises during the contraction phase, and then drops somewhat during the minor disruptions. The final major disruption, in which l_i drops by almost unity and the current profile becomes almost flat, occurs at about $t=6200\tau_A$.In Fig. 2 we show details from such a major disruption, simulated with 25 Fourier components, to improve on numerical resolution. The major disruption involves a sequence of events, the first of which is the "energy quench". This starts similar to a sawtooth. The m=1/n=1 mode is modified by the m=2/n=1 mode, as described in Sec. 3 for the minor disruptions. Furthermore, at the beginning of the modified sawtooth, the temperature is almost flat in the centre and falls off quickly outside the $q \approx 1$ region. Figure 2a is a contour plot of the electron temperature and a Poincaré plot of the magnetic field lines during the first phase of the energy quench. The region around the original q=2 and q=3/2 surfaces is stochastic, while the $q \approx 1$ region has good flux surfaces and shows a standard q=1 reconnection pattern. The modified sawtooth has a large content of m=3/n=2 magnetic perturbation, and at the end of the reconnection, the whole central region becomes stochastic over a short time (see Fig. 2b), by the simultaneous presence of high amplitude modes of different helicities. After this, there is a partial recovery of good flux surfaces in the centre, interrupted by another event similar to that in Fig. 2b. This time, q_0 rises sharply, and the m=2 mode continues to grow. The current profile now broadens quickly under the combined action of the m=2 mode and fine-scale turbulence. When the current profile becomes sufficiently broad, the m=3/n=1 mode grows

more or less on the Alfvén time-scale, and the internal inductance rapidly falls close to 1. During this phase, the negative voltage spike appears. Figure 2c shows a cross-section of the current profile and completely stochastic magnetic fields at this time.

Acknowledgement. This work was supported by JET under contract JW8/9007 and by the Swiss National Science Foundation.

REFERENCES

1. P.H. Rebut and B.J. Greene, IAEA Berchtesgaden 1976, Vol 2, 3.
2. J.A. Wesson, R.D. Gill, M. Hugon, et al, Nucl. Fusion **29**, 641 (1989).
3. A. Bondeson, Nucl. Fusion, Nucl. Fusion **26**, 929 (1986).
4. B.V. Waddell, B. Carreras, H.R. Hicks, et al, Phys. Rev. Lett. **41**, 1386 (1978).
5. M.F. Turner and J.A. Wesson, Nucl. Fusion **22**, 1069 (1982); K.I. Hopcraft and M.F. Turner, Phys. Rev. Lett. **56**, 2372 (1986).
6. S.P. Hirshman, R.J. Hawryluk, and B. Birge, Nucl. Fusion **17**, 611 (1977).
7. P.H. Rebut and M. Hugon, IAEA London 1984, Vol 2, 197.

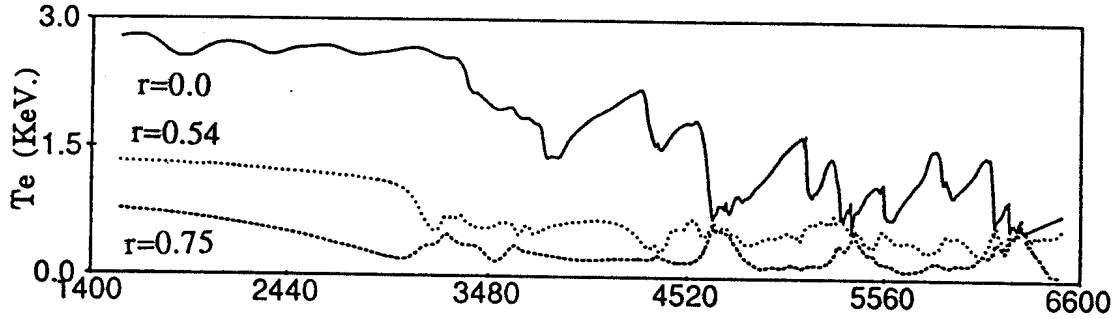

Figure1a. Time evolution of electron temperature at different radii.

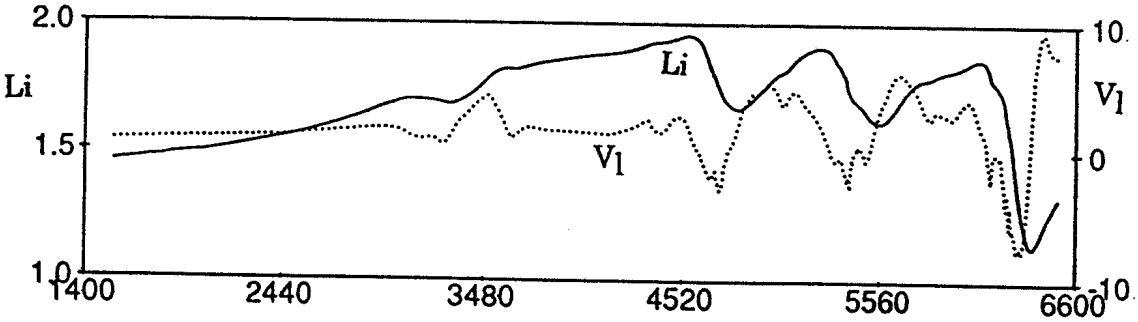

Figure 1b. Time evolution of internal inductance and loop voltage.

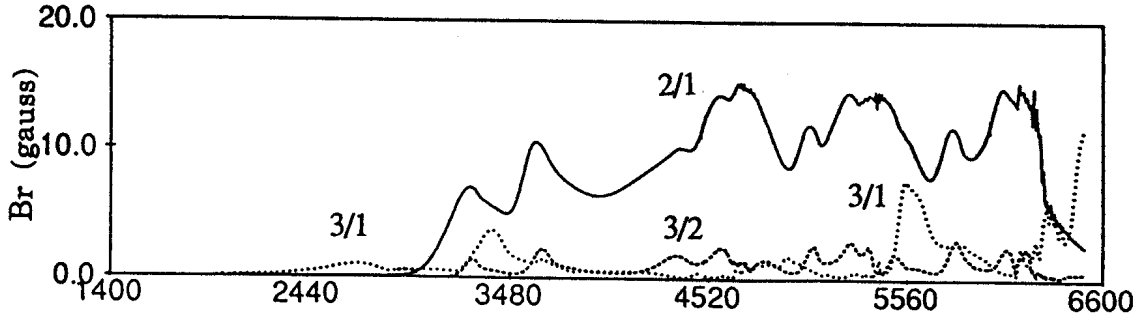

Figure 1c. Radial magnetic field at the wall; m=2/n=1, m=3/n=2, and m=3/n=1.

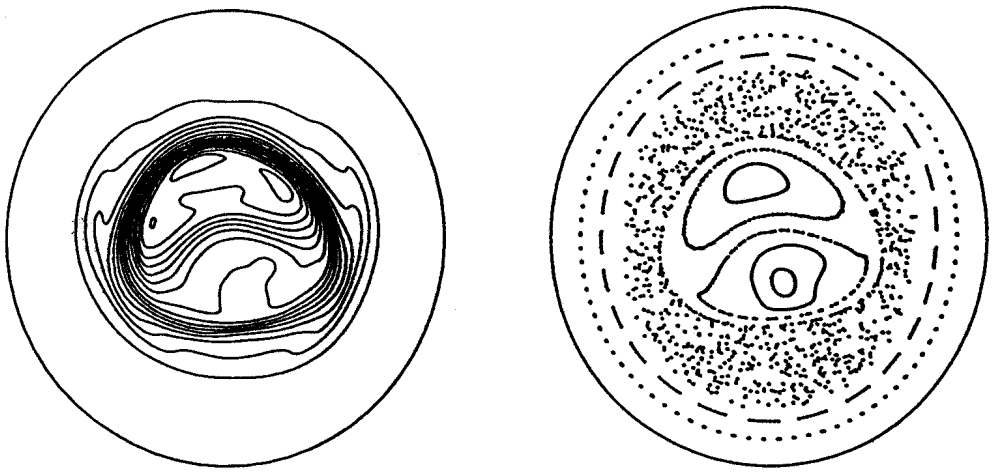

Figure 2a. Electron temperature and field lines during first stage of energy quench.

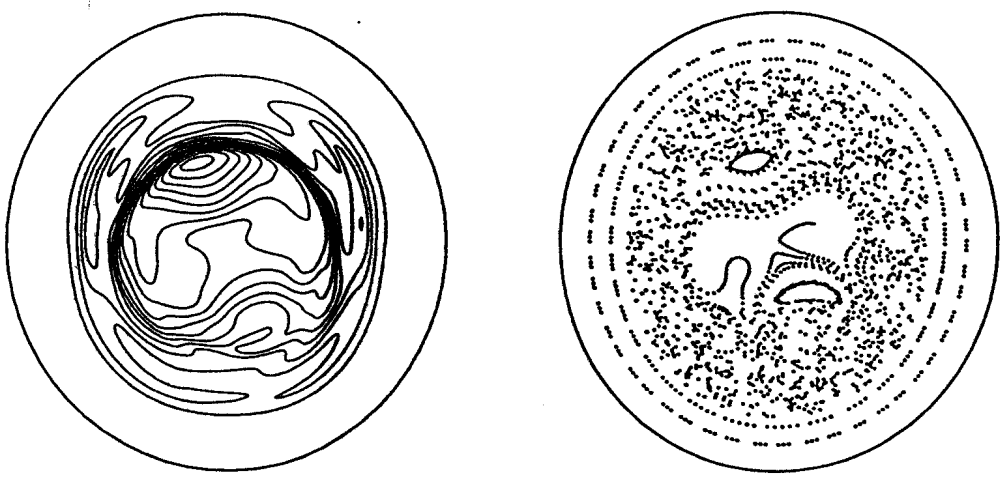

Figure 2b. Electron temperature and field lines at end of energy quench ($70\tau_A$ after 2a).

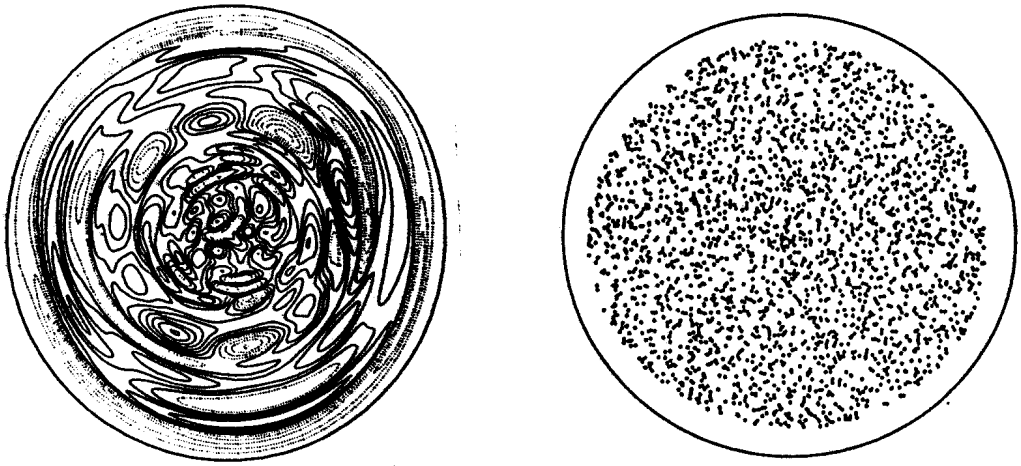

Figure 2c. Current density and field lines during voltage spike ($370\tau_A$ after 2a)

GLOBAL, RESISTIVE STABILITY ANALYSIS IN AXISYMMETRIC SYSTEMS

A. Bondeson[a], G. Vlad[b], and H. Lütjens[a]

[a]Centre de Recherches en Physique des Plasmas, Ass. Euratom-Confédération Suisse Ecole Polytechnique Fédérale de Lausanne, 21 Av. des Bains CH-1007 Lausanne, Switzerland.

[b]Associazione Euratom-ENEA sulla Fusione, C.R.E. Frascati, C.P. 65 - 00044 - Frascati, Rome, Italy.

1.INTRODUCTION

Numerical codes such as ERATO [1] and PEST [2] have played an important role in developing the understanding of ideal-MHD stability for tokamaks. These codes solve the linearized ideal-MHD eigenvalue problem without any ordering assumptions. For resistive MHD, similar codes have been developed only recently [3]. Under a collaboration between the CRPP Lausanne and ENEA Frascati, we have developed a resistive spectral code, MARS (MAgnetohydrodynamic Resistive Spectrum), for the full compressional MHD equations in two-dimensional geometry. Axisymmetric equilibria are computed by the cubic Hermite element code CHEASE, which allows specification of the pressure p and toroidal field, $T = RB_\phi$, or the surface averaged toroidal current, $I' = \langle J_\phi \rangle$, as functions of the poloidal flux ψ. The two codes use flux coordinates (s, χ, ϕ), where $s = (\psi/\psi_{edge})^{1/2}$ is the radial variable, ϕ the geometrical toroidal angle, and χ the poloidal angle, specified by choosing the Jacobian, J. MARS Fourier decomposes the components of v and **B** in χ and uses a finite difference scheme in the radial direction.

Here, we present results for a number of resistive instabilities where toroidal effects play an important role. All calculations are made with a fixed, and except where explicitly stated otherwise, circular boundary.

2. INTERNAL KINK

The properties of the n=1, internal kink mode differ strongly between a torus and a cylinder. For $q_0 < 1$, $q_{edge} > 1$, a finite aspect ratio cylinder is ideally unstable, independent of pressure, while the torus is *ideally* stable for $\beta_{pol} < \beta_{pcrit}$. At large aspect ratio, β_{pcrit} is independent of A = R/a, but depends on equilibrium profiles [4]. It has been shown recently [5,6] that at tight aspect ratio, even the *resistive* internal kink mode can be stable if the shear at the q=1 surface is sufficiently low. In Fig. 1 we show the growth-rate of the resistive internal n=1 mode as a function of aspect ratio for two different sequences of equilibria at zero β. The two sequences have different current profiles $I'(\psi)$ (both smooth functions of ψ) which are kept fixed, while the aspect ratio is varied. For Fig.1a, $I'(\psi)$ is monotonic, the q=1 radius is kept fixed at $r_{q=1} = 0.44a$, the central q is about 0.90 and the shear, $\hat{s} = r\, dq/dr$ at q=1, increases slightly with $\varepsilon_{q=1} = r_{q=1}/R$ from 0.20 to 0.25. Although the resistive growth-rate decreases with increasing ε, the resistive modes remain unstable down to very tight aspect ratio, $\varepsilon_{q=1} = 0.3$. The second sequence of equilibria (Fig. 1b) has less shear in the $q \le 1$ region and $dI'/d\psi = 0$ at the q=1 surface. Here $r_{q=1} = 0.62a$, $q_0 \approx 0.93$ and s ranges from 0.09 to 0.12, depending on aspect ratio. These equilibria are resistively stable for $\varepsilon_{q=1} > 0.25$. For $\eta < 10^{-6}$ and $\varepsilon_{q=1} < 0.15$, the growth-rates both in Fig. 1a and 1b follow the large-aspect-ratio scaling [6] for n=1 "m=1" tearing, $\gamma \propto \eta^{3/5} \varepsilon^{-8/5}$. For large η and small ε, the scaling is closer to that of the cylindrical resistive kink, $\gamma \propto \eta^{1/3} \varepsilon^{0}$. Triangularity, up to $\delta = 0.4$, has a negligible effect on the growth rates in the high-shear case, Fig.1a. In the case of lower shear (1b), triangularity is weakly stabilizing; $\delta = 0.3$ reduces the $\varepsilon_{q=1}$ needed for resistive stability from 0.25 to 0.21.

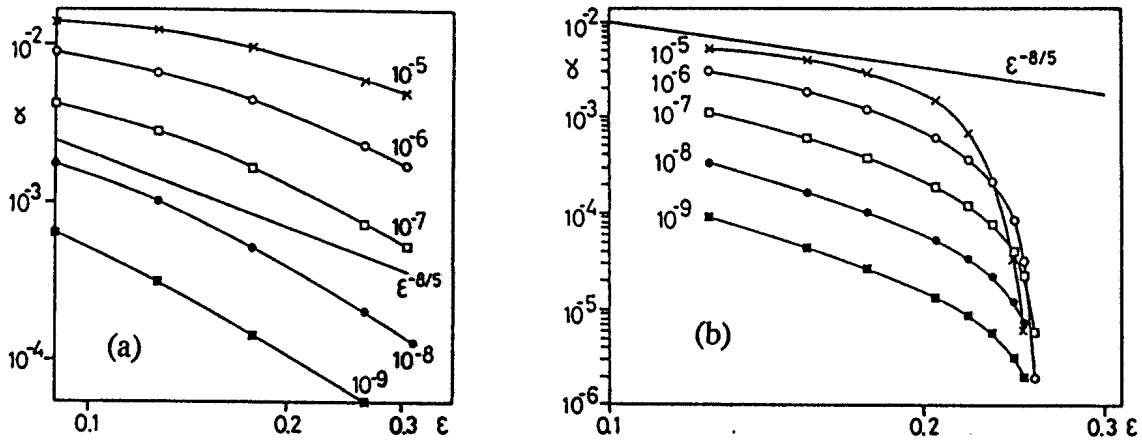

Fig. 1. Growth-rates of resistive internal kink mode as functions of aspect ratio for $\eta = 10^{-5}$, 10^{-6}, 10^{-7}, 10^{-8},and 10^{-9}. (a) $\hat{s}_{q=1} \approx 0.2$, (b) $\hat{s}_{q=1} \approx 0.1$.

Generally, in tokamaks, $\varepsilon_{q=1} < 0.25$, and, from TEXTOR, q_0 as low as 0.7 has been reported [5]. Under such conditions, resistive stability requires a local reduction of the shear at the q=1 surface [5] and a non-monotonic current profile. Figure 2 shows resistive growth-rates for an equilibrium with finite pressure and where the shear has a local minimum near the q=1 surface. For these equilibria, R/a = 2.5, $q_0 \approx 0.7$, $q_{edge} \approx 2.4$, and $r_{q=1} \approx 0.51a$. We used a non-monotonic current profile $\Gamma(\psi)$, and the shear profile for $\beta_{pol} = 0.13$ is shown in Fig. 2b. Figure 2a gives contours of equal growth-rate for $\eta = 10^{-7}$ as a function of β_{pol}, measured at the q=1 surface, and $q_i \equiv q(s=0.607)$, near the inflection point of q(s). Fig. 2a shows that the stable window in q_i is narrow and eventually shrinks to zero as β increases. Furthermore, the stable values of q_i increase with increasing β, which means that the q=1 surface moves inward into a region of somewhat higher shear. The apparent reason for this is that the ideal pressure driven mode is stabilized by global shear, and this effect competes with the requirement of low local shear for resistive stability. The resistive β-limit is therefore somewhat lower than the ideal one. The maximum value of $\beta_{pol}(q=1)$ reached with our profiles is 0.2, to be compared with the ideal limit of 0.3 for a parabolic q-profile [4].

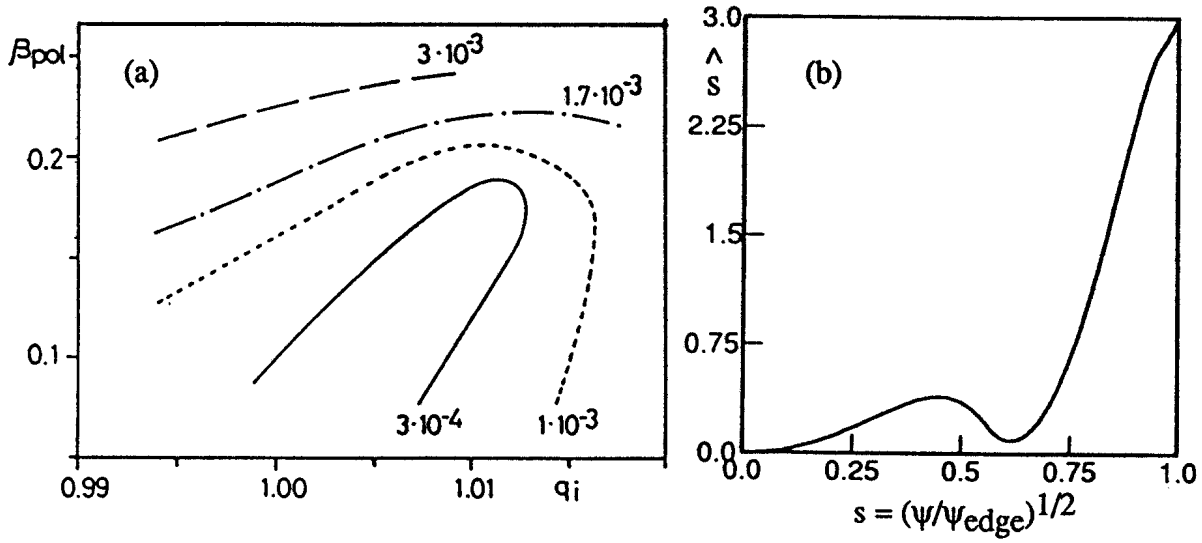

Fig. 2. (a) Growth-rate for resistive internal kink as a function of β_{pol} at q=1 and $q_i \equiv q(s=0.607)$, for a non-monotonic current profile with shear profile (b).

3. M ≥ 2 TEARING MODES AT FINITE BETA

Glasser, Greene and Johnson [7] showed analytically that the tearing mode is stabilized by favourable average curvature when β and $S = 1/\eta$ are sufficiently large. We have studied finite-β effects on the n=1 "m=2" tearing mode, using a current profile in the form of a rounded-off step-function, fixing A=2.5 and $q_0 = 1.5$ (strongly unstable to m=2 tearing in a cylinder) and varying the central β between 0.35 % and 2.45 %. (This made q_{edge} vary from 4.8 to 6.) The pressure at the edge was taken to be finite, at about 6 % of the central pressure p_0, while $p \approx 0.33\ p_0$ at the q=2 surface. The resistivity profile was inversely proportional to p. Figure 3a shows the real part of the growth rate as a function of central η for different β_0. Note that, for η above some value η_1,there are two purely growing modes which coalesce at $\eta = \eta_1$ and split into a pair with complex conjugate growth rates, which is unstable in a range $\eta_2 < \eta < \eta_1$, and finally becomes stable for $\eta < \eta_2$. The curves for different β in Fig 3 are almost identical if γ is scaled as $\beta^{3/2}$ and η as $\beta^{5/2}$, consistent with the simplified dispersion relation (88) for H = 0 in Ref.7. (For our equilibrium with $\beta_0 = 2.45$ %, in the notation of [7], $D_R \approx -0.16$ and $H \approx 0.08$ at the q=2 surface.) Clearly, high β is strongly stabilizing for resistive modes when the average curvature is favourable. Figure 3b shows the Fourier components of the perturbed magnetic field (with straight field-line Jacobian $J \propto R^2$)

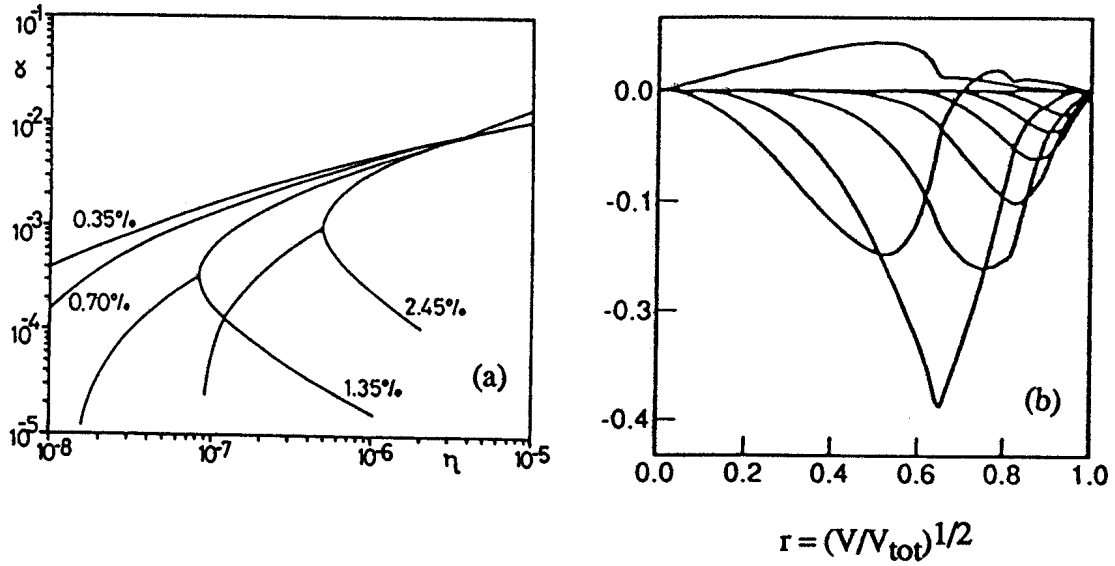

Fig.3 (a) Real part of growth-rate for "m=2", n=1 tearing mode for finite-β equilibria described in text. (b) Fourier components of $J\,\nabla s \cdot \mathbf{b}$ for the near marginal mode at $\eta = 1 \times 10^{-7}$ and $\beta_0 = 2.45$ %.

4. LOW-N RESISTIVE BALLOONING

Resistive ballooning modes are driven by pressure gradients in regions of unfavourable local curvature, and the ideal stabilization by field bending is reduced by resistivity. The resistive ballooning modes are, however, stabilized at sufficiently high S and large sound speed by fluid compression [8,9]. From the analytical theory of Ref. 9, we find that the pressure necessary for stabilization of high-n resistive ballooning modes scales with resistivity and pressure gradients as $\Gamma p_{stab} \propto \eta^{1/2}\,(dp/dr)^2$, where Γ is the adiabatic index (usually set to 5/3). We have verified with MARS that this scaling holds also for n=1 and n=2 modes. The

scaling implies that resistive ballooning modes will generally be unstable near the plasma boundary, where p is small and η large, unless dp/dr goes sufficiently rapidly to zero. (This is why we added a base pressure of $0.06p_0$ to separate tearing from resistive ballooning in Sec. 3.) It should be noted that resistive ballooning is stabilized in incompressible calculations where $\Gamma = \infty$. Fig. 4 shows the Fourier components of the velocity and magnetic field for an n = 2 resistive ballooning mode. The equilibrium has $q_0 = 1.02$, $q_{edge} = 2.5$, $\langle\beta\rangle = 2$ %, and a finite pressure gradient at the edge. The pressure at the edge has been raised to the point where the mode is marginally stable, $\beta_{edge} = 1.2 \times 10^{-3}$ with $\Gamma = 1$. The resistivity profile is given by $\eta(\psi) / \eta_0 = p_0 / p(\psi)$, with $\eta_0 = 1 \times 10^{-7}$, and the real frequency of the mode is about $9 \times 10^{-3}\ \omega_A$. Figure 4 shows that the velocity perturbations have a short radial wave-length, and are confined to the edge region. It is noteworthy, however, that the magnetic perturbations penetrate with a long radial wave-length to the centre of the plasma. Another interesting property, that can be seen from the radial variation of the complex amplitudes, is that near the plasma edge, the perturbations propagate radially outward. The mode involves a large number of different poloidal Fourier components and is thus strongly ballooning. It appears justified to speculate that modes of this type are responsible for transport in the edge region of tokamaks, and that their magnetic perturbations may contribute to transport also in the interior.

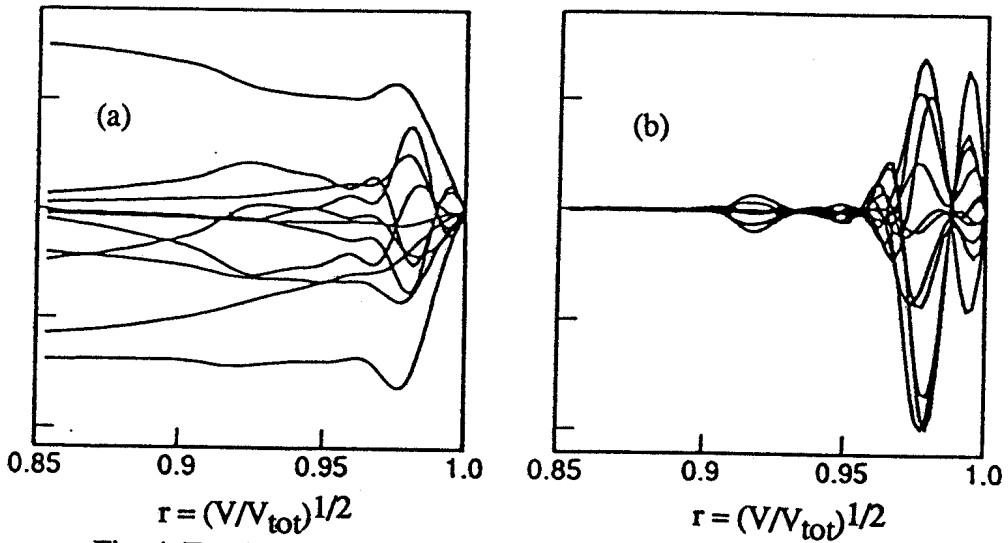

Fig. 4 Fourier components of radial magnetic field and velocity.
(a) $J \nabla s \cdot b$ and (b) $\nabla s \cdot v$ over outer 8 % of the minor radius.

REFERENCES

1. R. Gruber, F. Troyon, D. Berger, et al, Comp. Phys. Comm. **21**, 323 (1981).
2. R.C. Grimm, J.M. Greene, and J.L. Johnson, Meth. Comp. Phys. **16**, 253 (1976): J. Manickam, R.C. Grimm, and R.L. Dewar, Comp. Phys. Comm. **24**, 355 (1981).
3. L.A. Charlton, J.A. Holmes, H.R. Hicks, et al, J. Comp. Phys. **63**, 107 (1986).
4. M.N. Bussac, R. Pellat, D. Edery and J.L. Soule, Phys. Rev. Lett. **35**, 1638 (1975).
5. H. Soltwish, W. Stodiek, J. Manickam, et al , IAEA Kyoto (1986),Vol I, p. 263.
6. J.A. Holmes, B.A. Carreras, and L.A. Charlton, Phys. Fluids B **1**, 788 (1989).
7. A.H. Glasser, J.M. Greene, and J.L. Johnson, Phys. Fluids **19**, 567 (1976).
8. T.C. Hender, B.A. Carreras, W.A. Cooper, et al. Phys. Fluids **27**, 1439 (1984).
9. J.F. Drake and T.M. Antonsen, Jr., Phys. Fluids **28**, 544 (1985).

ALFVEN WAVE HEATING IN ASDEX

G.Besson, G.G.Borg, J.B.Lister, Ph.Marmillod.

Centre de Recherches en Physique des Plasmas
Association Euratom-Confédération Suisse
EPFL, 1015 Lausanne, Switzerland.

F.Braun, A.B.Murphy, J.-M. Noterdaeme, F. Ryter, and F.Wesner.

Max Planck Institut fur Plasmaphysik
Boltzmannstrasse 2, Garching bei Muenchen
Bundesrepublik Deutschland

An experiment has been completed on ASDEX to study the response of the plasma to Alfvén wave heating (AWH). Antenna excitation was provided by the old TCA rf generator with an output power capability of 500 kW. Two poloidal loop antennas were installed at the east and west ends of the tokamak allowing either N = 1 or N = 2 phasings. Since the largest antenna coupling to the Alfvén resonance is provided by the m = 1 surface wave, [1], the antennas consisted only of a single element on the low field side, whereas in TCA the antennas are located on the top and the bottom of the torus. The antenna elements consisted of 2 parallel bars of inductance 730 nH and, as in TCA, were left unshielded [2]. A typical antenna circulating current of 2 kA peak at 1.80 MHz was provided for the experiments.

The excited wave spectrum consisted of discrete Alfvén wave (DAW) peaks separated by a featureless wave continuum (see the wavefield trace in Fig. 3); characteristic of the spectrum already observed in TCA [1]. A dispersion plot of density versus toroidal field is shown in Fig. 1 for the (n,m)=(2,1) DAW. The curve on the left shows the characteristic dependence on Alfvén speed and the curve on the right shows the location of the (2,1) DAW with respect to the (2,0) and (2,1) continuum thresholds. In addition to the Alfvén spectrum at the fundamental frequency, a spectrum of harmonic waves is also excited in the plasma edge as in TCA [2].

A typical plasma response to AWH is shown in Fig. 2 for 1 kA peak (approx) in the antenna and 50 kW delivered to the plasma. The Alfvén pulse occurs at 2.1 s and lasts 400 ms. During this pulse the most important plasma effect is an

uncontrolled density rise. Profile measurements of Z_{eff} revealed that the density rise is not due to impurities. Even though the loop voltage is observed to increase at the beginning of the rf, it tends to decrease later in the pulse. No observable change in the charge exchange flux of low energy neutrals and a general decrease in H_α (Fig. 3) at the time of the rf pulse suggests that a change in recycling is not responsible. These conclusions have already been suspected from previous AWH experiments in TCA and are now known to be independent of whether or not the antennas are electrostatically shielded [2]. The density rise is accompanied by increases in $\beta + l_i/2$, β_{dia}, P_{rad}, T_e, T_i and plasma energy. The maximum power that could be delivered to the plasma (450 kW approx.) was limited by plasma disruption.

An interesting effect of AWH is the so called spectral discontinuity observed on certain plasma parameters. An example is shown in Fig. 3 (I_p = 400 kA) where the density rises and breaks just after a DAW at 1.3 s. The effect on the plasma appears to be a sudden decrease in energy and particle confinement.

The heating analysis has always been complicated by the effects of the increasing plasma density. Strong electron heating has been observed using Thomson scattering [3], however the effect of AWH is to increase the saw tooth amplitude and not the base temperature compared with the ohmic temperature at the same density. From the plasma energy calculated from the diamagnetic loop, one can compare the heating during rf with that of gas puffs which give rise to a similar density increase in the same shot. An example is shown in Fig. 2 where a gas puff density rise occurs between 0.9 and 1.2 s. A set of plasma energy loci versus density are shown in Fig. 4. Although it was a general result of the experiments that the effect of rf on the plasma was largest at lowest density, there is no significant qualitative difference between gas puffing and AWH. However a more detailed set of observations than these is required to observe separate heating.

Finally, a series of experiments with AWH applied during a long 1 MW NBI pulse failed to produce any observable effect in addition to that of NBI. The density rise observed with AWH into ohmic discharges was absent, although the coupling may be reduced by changes in the edge profiles during NBI.

REFERENCES

[1] Collins G.A., Hofmann F., Joye B. et. al. Phys. Fluids, **29**, 2260 (1986).
[2] Borg G.G. and Joye B. *'An experimental study of Alfvén wave heating using electrostatically screened antennas in TCA'*. Paper presented at this conference.
[3] Joye B., Lietti A., Lister J.B. et. al. Phys. Rev. Letters, **56**, 2481 (1986).

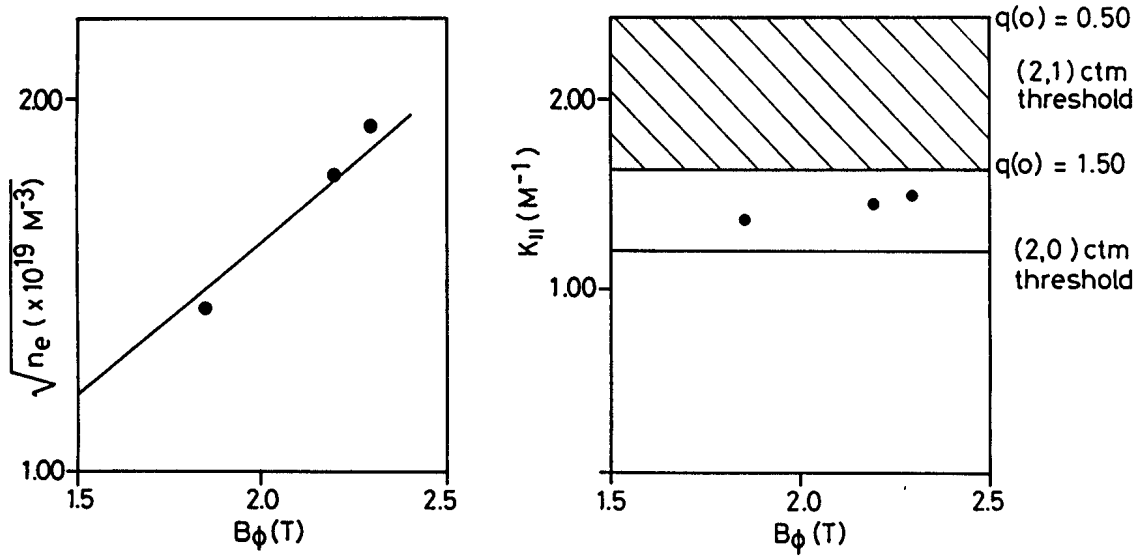

Fig. 1. Plot of the dispersion relation in the density-toroidal field plane for the (2,1) DAW.

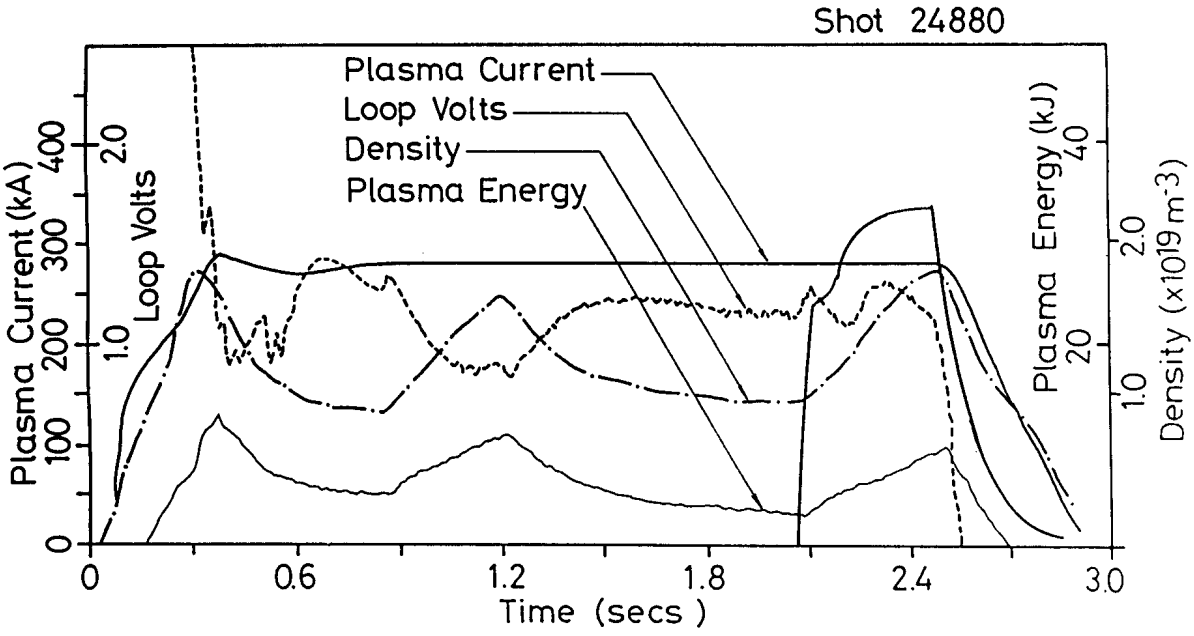

Fig. 2. A typical discharge in ASDEX with a gas puff at 0.9 s and an AWH pulse at 2.1 s.

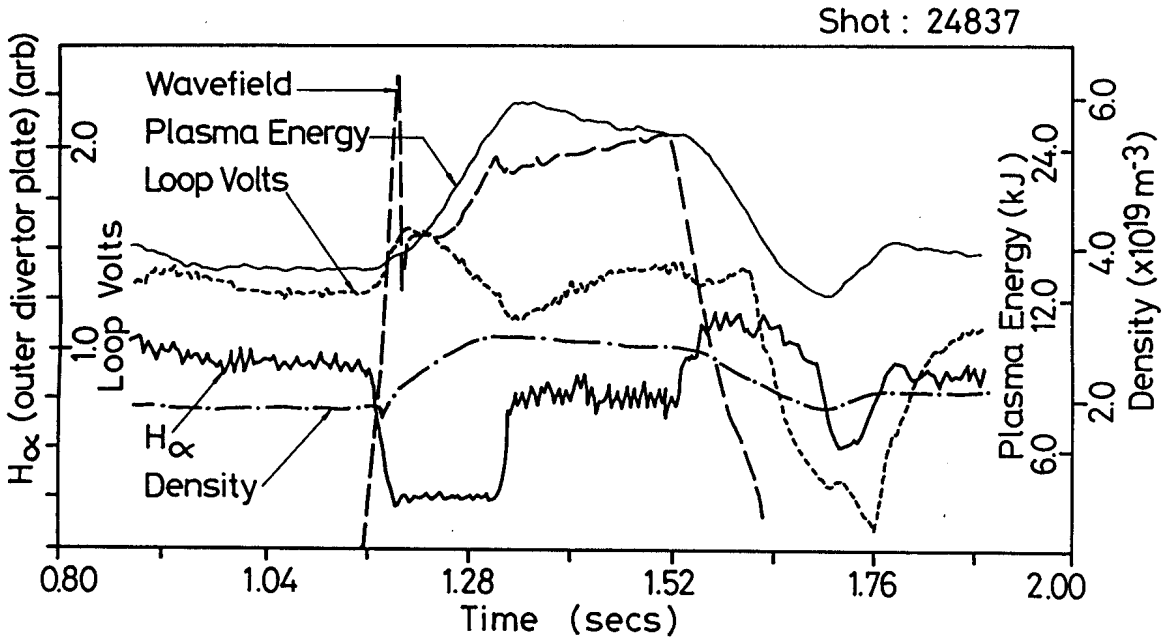

Fig. 3. Shot showing the effect on plasma energy, density ,loop volts and H_α emission during a spectral discontinuity.

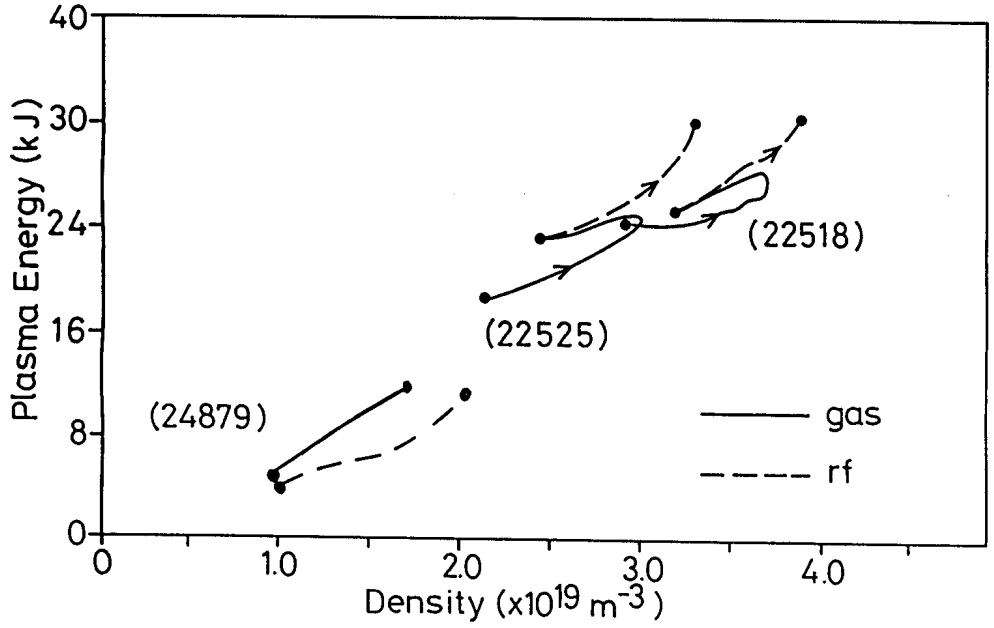

Fig. 4. Comparison of plasma energy versus density for gas puffs and AWH pulses for various plasma conditions

AN EXPERIMENTAL STUDY OF ALFVEN WAVE HEATING USING ELECTROSTATICALLY SHIELDED ANTENNAS IN TCA

G.G. Borg and B. Joye

Centre de recherches en Physique des Plasmas
Association Euratom-Confédération Suisse
EPFL, 1015 Lausanne, Switzerland

Despite the wide acceptance of electrostatic screens in ICRH for the protection of the plasma from the near fields of rf antennas, it has always been considered that low voltages at low frequency have made such screens unnecessary in Alfvén wave heating (AWH) [1]. Despite this, AWH performs rather poorly as a heating method; the results being confused by a density rise up to 300% of the target density. It is now known that the density increase arises neither from impurity injection nor from a change in recycling. In addition, an extensive range of phenomena have been observed in the plasma scrape-off layer (SOL). During AWH, the SOL density is observed to decrease, the SOL floating potential is perturbed in a way that reflects the Alfvén wave spectrum, the antennas charge negatively and draw a large current from the plasma and harmonics have been observed on the edge wave fields. The cause and correlation of these effects with each other and their impression on the bulk plasma response was not known.

Experimental results from the TORTUS tokamak [2] have indicated that the density increase might be eliminated by electrostatic screens. In their case, two AWH experiments were performed. In the first, an unshielded OFHC copper loop antenna was excited at a given power and, in the second, the same antenna was excited at the same power after installation of an aluminium, TiN coated, slotted screen. The density increase in the first case was shown to be completely eliminated in the second, although spectroscopic measurements revealed a difference in the plasma O(II) and Cu(I) content for each case.

Recently, electrostatic screens have been installed in TCA. TCA has four pairs of top and bottom antennas in each quadrant of the torus which are excited at 2 MHz. Each antenna consists of 6 parallel poloidal bars fed in push-pull. Screens were only installed on two pairs of antennas. On antenna top and bottom pair (1,5), the screens consist of a capacitive divider of 11 earthed blades parallel to the toroidal field and a fully grounded side limiter at the front and back of each antenna. The screens were made of the same material as the antenna, stainless steel, to avoid a possible confusion in the interpretation of experimental results due to impurities. On antenna pair (2,6) the screens are identical except that the blades are not earthed. This permits a comparison to be made between electrostatic and floating screens for identical conditions of plasma coupling. The

screens do not significantly alter the antenna near magnetic field. Antenna pairs (3,7) and (4,8) were left unshielded. The experimental arrangement is shown in Fig. 1.

Some physical quantities measured in the SOL are shown in Fig. 2 for excitation of antenna pair (3,7) (Fig. 2a) and antenna pair (1,5) (Fig. 2b) with a similar antenna current. The natural polarisation V_{pol}, probe floating potential V_{flot}, measured on unexcited antenna 4, and ion saturation current I_{sat}, measured by applying negative polarisation to antenna 4, have all been significantly reduced by the screens. In addition, the current drawn from the plasma by the antennas was completely eliminated. The poloidal wave field component detected by a pick up coil in the SOL is shown plotted in the complex plane during the passage of a discrete Alfvén wave [1]. There is evidently no clear effect of screens on the relative amplitude of the first harmonic (4 MHz) and the fundamental (2 MHz) component; thus eliminating a possible explanation of the harmonics in terms of a Langmuir interaction between the antenna and the SOL plasma. From these results one can simply conclude that the basic technical requirement of the screens has been met. We also mention that there is no differernce observed in the results for antenna pairs (1,5) and (2,6).

Results for the average plasma parameters are shown in Fig. 3, including an ohmic discharge (Fig. 3d) for reference. Comparison of the case for excitation without screens (antenna pair (3,7) in Fig. 3a) and with screens (antenna pair (1,5) in Fig. 3b and pair (2,6) in Fig. 3c) reveals very little difference in the response of any of the plasma parameters that cannot be attributed to the difference in antenna power for each case. In particular, the density increase, which is known to scale with rf power and be almost entirely responsible in itself for the observed changes in $\beta + l_i/2$ and the soft X-ray flux, has not been significantly reduced by screens.

In conclusion, we note that the main benefit of screens in AWH is to 'clean up' most parasitic phenomena from the plasma SOL which are, without doubt, linked to the direct contact between the plasma and the unshielded antenna. This benefit, however, does not, in any way, for better or for worse, alter the plasma bulk response to AWH. The separate challenges to reveal the origin and importance of the harmonics and to comprehend the response of a tokamak plasma to high power Alfvén waves still remain.

References

[1] Collins G. A., Hofmann F., Joye B. et. al. Phys. Fluids, **29**, 2260 (1986).
[2] Ballico M.J., Brennan M.H., Cross R.C. et. al. Plas. Phys. and Contr. Fus. **30**, 1331 (1988).

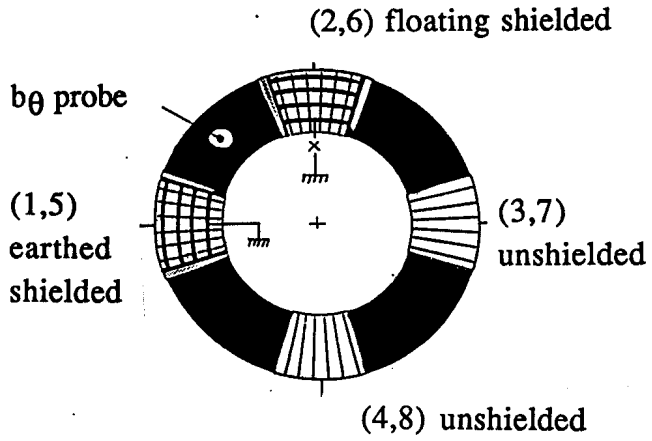

Fig. 1. Top view of TCA showing the antennas and the wave probe.

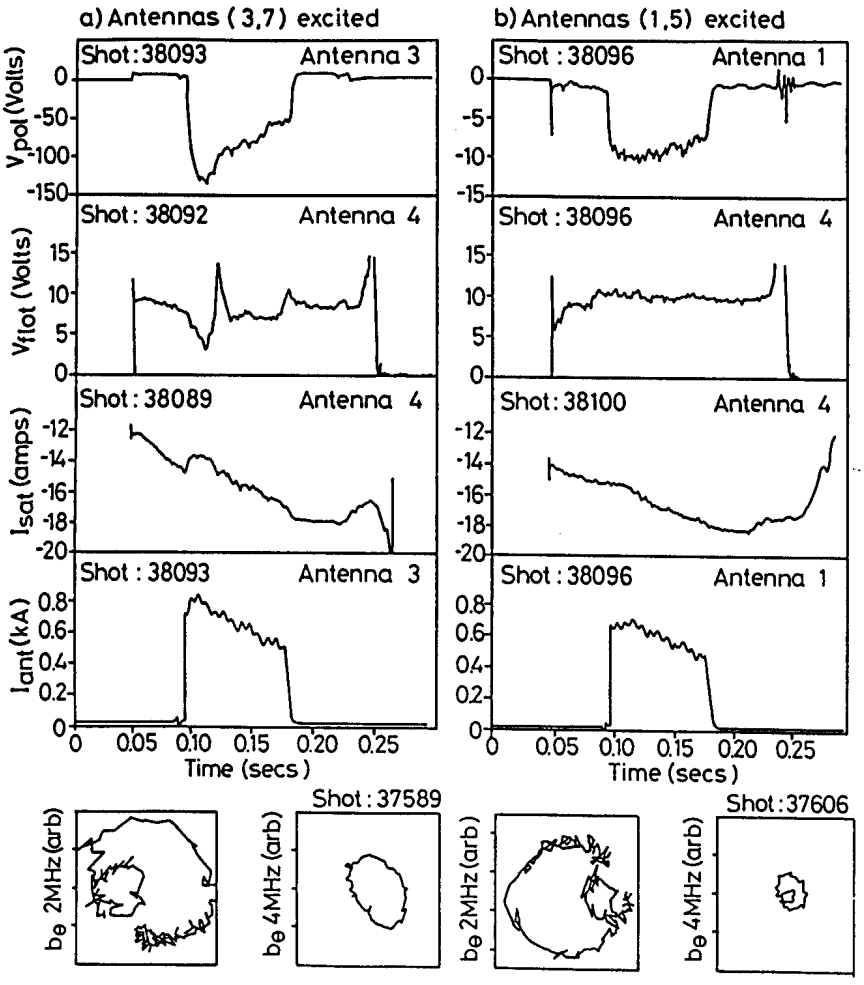

Fig.2. Effects of rf on the SOL, during AWH with a) unshielded antenna pair (3,7) and b) shielded antenna pair (1,5).

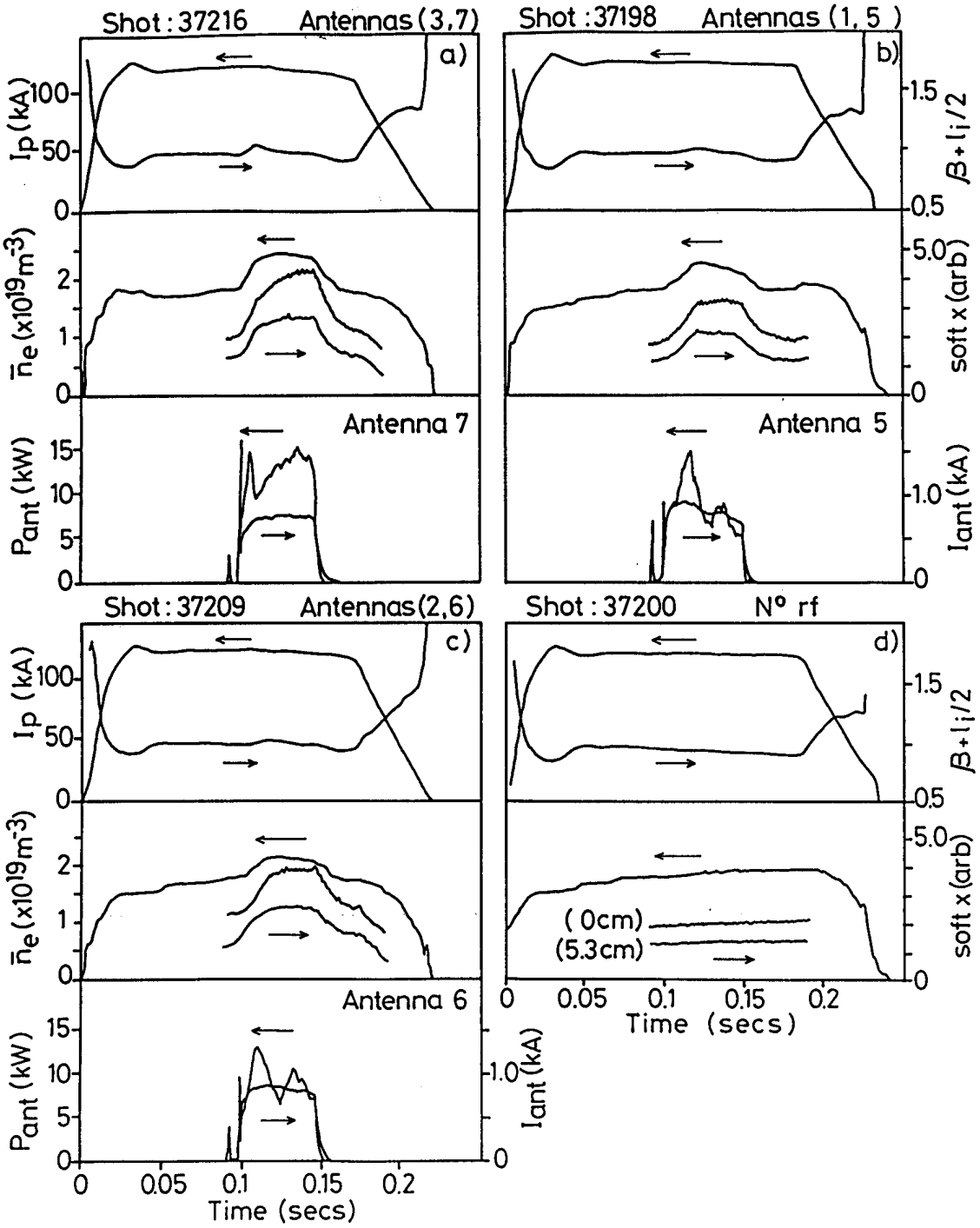

Fig. 3. Effect of rf on the average plasma parameters during AWH with a) unshielded antenna pair (3,7), b) earthed, shielded antenna pair (1,5), c) floating, shielded antenna pair (2,6) and without AWH, d).

DYNAMIC RESPONSE ANALYSIS AS A TOOL FOR INVESTIGATING TRANSPORT MECHANISMS

Th. Dudok de Wit, B. Joye, J.B. Lister, J.-M. Moret*

Centre de Recherches en Physique des Plasmas
Association Euratom-Confédération Suisse
Ecole polytechnique Fédérale de Lausanne
CH-1015 Lausanne, Switzerland

* present address : CEN Cadarache,
13108 St. Paul-lez-Durance, France

I) Introduction

Dynamic response analysis provides an attractive method for studying transport mechanisms in tokamak plasmas. The analysis of the radial response has already been widely used for heat [1,2] and particle transport [3] studies. The frequency dependence of the dynamic response, which is often omitted, reveals further properties of the dominant transport mechanisms. Extended measurements of the soft X-ray emission were carried out on the TCA tokamak in order to determine the underlying transport processes.

II) Dynamic response analysis

The transport processes are investigated by sinusoidally modulating the gas valve opening or the Alfvén RF power amplitude and measuring the subsequent perturbation on the soft X-ray emission. The profiles are obtained from an Abel-inversion of the signals of a 15 channel pinhole camera. The experiments are carried out in the TCA tokamak ($R=0.61$ m, $a=0.18$ m, $I_p \leq 130$ kA, $B_\phi=1.51$ T, $n_e \leq 10^{20}$ m^{-3}) for a frequency range of 30 to 600 Hz, which roughly corresponds to the inverse particle confinement time. We thereafter express the dynamic response of the modulated signals by their relative amplitude and their phase with respect to the external perturbation.

III) Analysis of the soft X-ray emission

Previous results [4] show that both RF power and gas valve modulation lead to a similar response of the soft X-ray emission. Even if a fraction of the RF power is directly thermalised, the large density increase which is simultaneously induced dominates the observed dynamic response. This response is characterised by a discontinuity at mid-radius, fig. 1. A minimum in the phase profile indicates the presence of a local source from which the perturbation emanates. Operation at different plasma currents reveals that this effective source moves with the sawtooth inversion radius. The resulting perturbation displays a fast inward propagation due to sawtooth activity. The outward propagation is

however considerably delayed, which leads to a phase jump, fig. 1.

In order to determine the origin of the observed modulation of the soft X-ray flux, we consider the different parameters which compose it :

$$A = f(Z_{eff})\, n_e^2\, T_e^{\alpha} \tag{3.1}$$

The function $f(Z_{eff})$ is roughly proportional to the impurity concentration and $\alpha = 2\text{–}8$ is the temperature exponent. For small perturbations, we obtain :

$$\frac{\tilde{A}}{\bar{A}} = \frac{\tilde{f}}{\bar{f}} + 2\frac{\tilde{n}_e}{\bar{n}_e} + \alpha\frac{\tilde{T}_e}{\bar{T}_e} \tag{3.2}$$

Measurements of the density profile show that gas valve and RF power modulation create an inward propagating density pulse. Inside the inversion radius, the density and the soft X-ray perturbations are synchronous, fig. 1. Since their relative amplitudes are in a ratio of 1:3, we conclude that a large fraction of the soft X-ray modulation can be attributed to the electron density. Outside the inversion radius however, the picture completely changes, in that both perturbations move in different directions and have a different amplitude ratio. A possible explanation would be that the soft X-ray response is due to either a heat pulse or an impurity flux. Experiments are being carried out in order to determine which effect predominates.

We conclude that the modulation of the soft X-ray emission profile inside the inversion radius can be ascribed to a density modulation, whereas impurity or heat modulation may dominate outside the radius. The perturbation emanating from the inversion radius would be triggered by a change in the density profile gradient.

IV) Transport model

In order to identify the dynamic response analysis to an underlying transport process, we consider two widely used transport models and calculate the resulting dynamic response. The modulated parameter $x(r,t)$ can either be the electron temperature, the density or the impurity concentration since all of these require similar transport equations.

Firstly, convection is taken to be the dominant process, with a spatially constant convective velocity

$$\frac{\partial x}{\partial t} = \frac{1}{r}\frac{\partial}{\partial r}\left(r^2 v \frac{x}{a}\right) + S \tag{4.1}$$

Using the Ansatz

$$x(r,t) = \bar{x}(r) + \tilde{x}(r)\, e^{-j\omega t} \tag{4.2}$$

a solution of the source-free interior of the plasma is obtained

$$\tilde{x}(r) = \frac{\tilde{x}_o}{r^2}\, e^{-\frac{j\omega a \log(r)}{v}} \tag{4.3}$$

The phase can then be expressed as

$$\angle\tilde{x} = \angle\tilde{x}_o - \frac{\omega a \log(r)}{v} \tag{4.4}$$

Such a linear frequency dependence is characteristic of a perturbation which propagates with a pure time delay.

Secondly, we consider a diffusive process

$$\frac{\partial x}{\partial t} = \frac{1}{r}\frac{\partial}{\partial r}\left(rD\frac{\partial x}{\partial r}\right) + S \qquad (4.5)$$

which has the homogeneous solution :

$$\tilde{x}(r) = \tilde{x}_o J_o(kr) \quad \text{with} \quad k = \sqrt{j\omega/D} \qquad (4.6)$$

In general the condition

$$kr >> 1 \qquad (4.7)$$

is satisfied, so that the phase can be approximated by

$$\angle\tilde{x} = \angle\tilde{x}_o + \sqrt{\omega r^2/2D} \qquad (4.8)$$

If a radial variation of the transport coefficients is included, the radial dependence in equations (4.4) and (4.8) changes but the frequency dependence is not affected. Hence a measurement of the phase at different frequencies allows to determine whether convection or diffusion is the dominant transport process. Although the amplitude spectrum can be used in a similar way, we omit it since it requires an absolute calibration.

V) Frequency dependence of the dynamic response

A plot of the soft X-ray emission phase versus the modulation frequency reveals a clear quadratic dependence, fig. 2. This dependence is most evident between 100 and 400 Hz. Below this range, condition (4.7) no more holds. The same dependence reappears when the phase reference is the flux at r=0.088m instead of the RF power. Using equation (4.8), a uniform diffusion coefficient can be obtained inside the inversion radius :

$$D = 1.23 \pm 0.2 \ m^2s^{-1}$$

This value is about twice the global particle diffusion coefficient. We conclude that the response of the soft X-ray emission to density modulation is dominated by diffusive processes, both inside and outside the inversion radius.

The frequency dependence of the phase profile allows us to further characterise the transport mechanisms. The large phase shift observed just outside the inversion radius was first attributed to a local barrier similar to the thermal insulating layer observed on TFR at the q=1 surface [5]. If this phase shift were due to reduced transport coefficients, it would increase indefinitely with the modulation frequency. Instead, the observed shift saturates at a value below 180°, fig. 2, which is characteristic of a power dipole (source/sink term). This dipole can be explained by local change in the diffusion coefficient at the sawtooth inversion radius as confirmed by a 1-D simulation code. The strong link between this local modulation and the inversion radius suggests that the change in the transport is due to a modification of the sawtooth activity.

VI) Conclusion

Transport mechanisms have been investigated by measuring the dynamic response of tokamak ohmic plasmas to perturbations such as gas valve or RF power modulation. The observed response of the soft X-ray flux can be attributed to a perturbation which starts at the inversion radius and is triggered by a change in the

density profile gradient. Extended measurements of the frequency dependence reveal the dominant nature of diffusive processes and also show a discontinuity in the transport which is due to sawtooth activity.

References

1) Alikaev V. et al., Plasma Physics and Contr. Fusion **29** (1987) 1286.
2) Lebeau D., Koch R. et al., proc. 16th EPS conference, Venice 1989, **III**, 1061.
3) Gentle K.W. et al., Plasma Physics and Contr. Fusion **29** (1987) 1077.
4) Joye B. et al., Plasma Physics and Contr. Fusion **30** (1988) 743.
5) TFR group, Nuclear Fusion **26** (1986) 849.

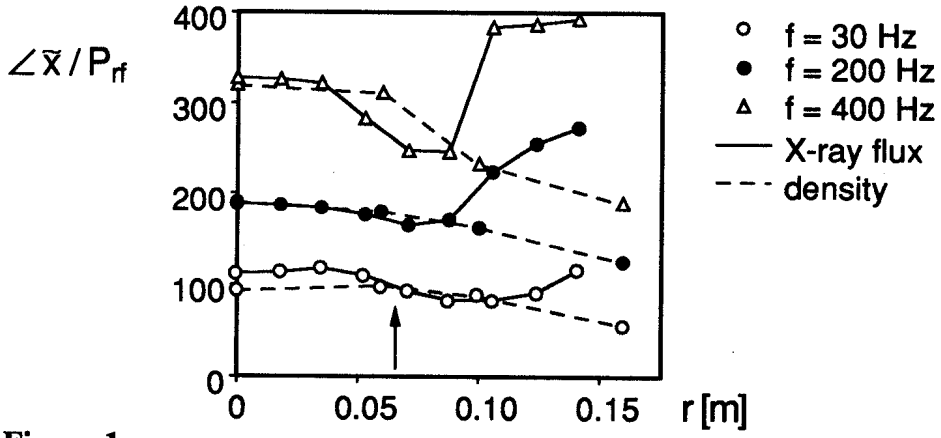

Figure 1
Phase profiles of the perturbed Soft X-ray emission and electron density during RF power modulation, as measured for different modulation frequencies at q(a)=3.1. The arrow indicates the position of the inversion radius. The profiles are symmetric with respect to the centre of the plasma.

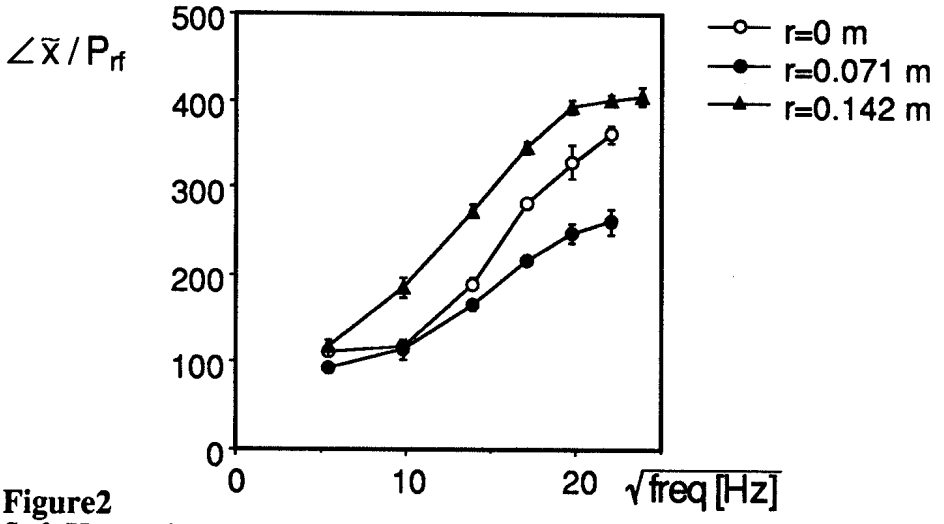

Figure2
Soft X-ray phase response as a function of the square root of the modulation frequency, taken at three radial positions : in the centre, at the inversion radius, and near the plasma edge.

PARTICLE TRANSPORT STUDIES ON TCA USING THE DYNAMIC RESPONSE OF THE EFFECTIVE MASS

Th. Dudok de Wit, B.P. Duval, B. Joye, J.B. Lister

Centre de Recherches en Physique des Plasmas
Association Euratom-Confédération Suisse
Ecole polytechnique Fédérale de Lausanne
CH-1015 Lausanne, Switzerland

I) Introduction

Particle tagging in a tokamak provides an attractive method for studying transport mechanisms. The injection of test particles at the plasma edge and the subsequent measurement of their concentration at the centre can be used to quantify the underlying transport mechanisms. This was done on the TCA tokamak by injecting hydrogen into a deuterium discharge, and simultaneously measuring the temporal evolution of the central effective mass and the edge ionisation rate.

II) Measurement of the effective mass

For different species of ions with mass A_i and density n_i, the effective mass can be defined as the number of nucleons per free electron :

$$A_{eff} = \sum_k \frac{n_i}{n_e} A_k \qquad (2.1)$$

Typical values are 1 for hydrogen only, 2 for deuterium and close to 2 for most fully stripped impurities. Hence for clean plasmas, a real-time measurement of A_{eff} provides a measurement of the ratio of hydrogenic species.

The effective mass at the plasma centre is measured by frequency tracking a global Alfvén wave during the plasma current flat-top (R=0.61 m, a=0.18 m, $I_p \leq 170$ kA, $B_\phi = 1.51$ T, $\bar{n}_e \leq 10^{20}$ m^{-3}). The diagnostic, described in [1], gives A_{eff} in real-time with an accuracy of 3% and a temporal resolution < 0.2 ms. Numerical simulations show that the measured mass is heavily weighted by the centre of the plasma [2].

The hydrogen and deuterium recycling rates at the plasma edge are inferred from the intensity of the H_β and D_β lines as measured by a visible spectrometer. The spectrum is repetitively integrated and acquired every 2-3 ms. This limits the temporal resolution of the diagnostic.

The ratio of the intensities of the lines yields a measurement of the incremental effective mass, which we define as :

$$R_A = 1\frac{I_H}{I_H+I_D} + 2\frac{I_D}{I_H+I_D} \qquad (2.2)$$

Since the impurity concentration was always small, and the following analysis is based

on changes of R_A, impurities can be neglected and ΔR_A is proportional to the change in the effective mass at the plasma edge.

III) Dynamic response analysis

The diagnostics described both provide a well-localised measurement and allow a simultaneous monitoring of the mass change at the plasma edge and at the centre. In this experiment we puff hydrogen into deuterium plasmas and measure the subsequent change in R_A and A_{eff}, fig. 1. For relatively small density increases ($\Delta n_e/n_e \lesssim 30\%$) the measured mass changes are proportional to the local density of the injected gas. We therefore conclude that the dynamic response of the central effective mass to the edge incremental mass is governed by the particle transport of the injected species.

Several methods allow us to study the dynamic response of A_{eff} to R_A. In order to retain the maximum amount of information, we extract the transfer function by performing a system identification analysis [3] :

$$H(\omega) = \frac{\Delta A_{eff}}{\Delta R_A} \tag{3.1}$$

This transfer function is most easily expressed by its gain $|H(\omega)|$ and its phase $\angle H(\omega)$. These are given over a continuous frequency range ($0 < f < 1/2\tau$, τ is the temporal resolution) and determine the underlying particle transport mechanisms. Next, we compare this experimental transfer function with the one obtained from a particle transport model.

IV) Particle transport model

We assume that the transport of the injected gas can be described by a simple model which includes spatially uniform diffusion coefficient and convective velocity [4] :

$$\frac{\partial n_k}{\partial t} = \frac{1}{r}\frac{\partial}{\partial r}\left(rD\frac{\partial n_k}{\partial r}\right) + \frac{1}{r}\frac{\partial}{\partial r}\left(r^2 v\frac{n_k}{a}\right) + S(r) \tag{4.1}$$

The effect of the injected gas is analysed as a time-dependent perturbation of its density :

$$n_k(r,t) = \bar{n}_k(r) + \tilde{n}_k(r)e^{-j\omega t} \tag{4.2}$$

The homogeneous solution of equation 4.1 is a confluent hypergeometric function :

$$\tilde{n}_k(r) = \tilde{n}_{ko}\, M\left(-\frac{j\omega a}{2v}, 1, \frac{vr^2}{2aD}\right) e^{-\frac{vr^2}{2aD}} \tag{4.3}$$

so that the transfer function becomes :

$$H(\omega) = \frac{\tilde{n}_k(r=0)}{\tilde{n}_k(r=a)} = {}^{1}\Big/{M\left(-\frac{j\omega a}{2v}, 1, \frac{va}{2D}\right)} e^{-\frac{va}{2D}} \tag{4.4}$$

which for the range of v and D values considered here can be approximated by a Bessel function :

$$H(\omega) \approx e^{\frac{va}{4D}} \Big/ J_o\left(\sqrt{\frac{va}{D} + \frac{j\omega a^2}{D}}\right) \qquad (4.5)$$

This simple model adequately reproduces the measured transfer function, fig. 2. A non-linear optimisation routine is further used to estimate v and D by minimising the phase and gain differences between the measured and the calculated transfer function. The frequency dependence of the amplitude and the phase is dominated by the value of the diffusion coefficient, whereas the convective velocity mostly determines the average amplitude. Due to the good parameter sensitivity of the diffusion coefficient, the highest accuracy is achieved for D. Its statistical measurement error is typically 10%. The value of v however is more difficult to extract, since it is very sensitive to the absolute calibration of the diagnostics; in general, the accuracy is 0.8 ms^{-1}.

V) Experimental Results

The dynamic response measurements were made for two different conditions which have important implications on the validity of the measured particle transport.

1) First results, in an unconditioned tokamak, indicated that a negligible fraction of the injected hydrogen was absorbed by the vessel wall. Since we could therefore assume particle conservation, the mass measurement could be used to determine the hydrogen transport coefficients. Measurements at q_a=3.1, $\bar{n}_e$= 3–5·10^{19} m^{-3} gave the following results :

$$D = 0.58 \pm 0.04 \ m^2s^{-1}$$
$$v = 0.57 \pm 0.83 \ ms^{-1}$$

For comparison, results obtained under similar conditions from particle balance equations and laser ablated impurity injection [5] gave :

$$D_{pb} = 0.70 \pm 0.20 \ m^2s^{-1}$$
$$D_{abl} = 0.73 \pm 0.10 \ m^2s^{-1}$$ respectively.

We note that $D_{pb} > D$, which implies that the central mass change is due to a diffusion of the injected gas as well as the plasma working gas, as one would expect.

2) Other experiments were performed in a tokamak in which a film of boron carbide had been deposited. This film appeared to significantly enhance the working gas absorption by the vessel, accompanied by a partial release during subsequent discharges [6]. Under these conditions, particle conservation was no longer satisfied. The edge incremental mass was no longer measured by the H_β and D_β line intensities which were more influenced by local edge recycling. The absence of this measurement prohibited our analysis.

VI) Conclusion

The dynamic response of the effective mass provides a novel and attractive method of increasing our knowledge of transport of an isotope of the working gas injected into a plasma. In conditions in which the absorption at the tokamak vessel wall was small, the method has been used to estimate separately the diffusive and the convective transport coefficients. The measured values are consistent with those obtained from global particle balance equations.

References

1) Th. Dudok de Wit, J.B. Lister, B.P. Duval et al., *Central mass feedback control using the Discrete Alfvén Wave spectrum*; accepted in Nuclear Fusion.
2) G.A. Collins, A.A. Howling, J.B. Lister et al., Plasma Phys. Contr. Fusion **29** (1987) 323.
3) Söderström T., Stoica P., *System identification*, Prentice-Hall, New York, 1989.
4) K.W. Gentle, B. Richards, F. Waelbroeck, Plasma Phys. Contr. Fusion **29** (1987) 1077.
5) B.P. Duval, private communication.
6) Th. Dudok de Wit, B.P. Duval, Ch. Hollenstein, B. Joye, *Effects of boronisation on the plasma parameters in TCA*; presented at this conference.

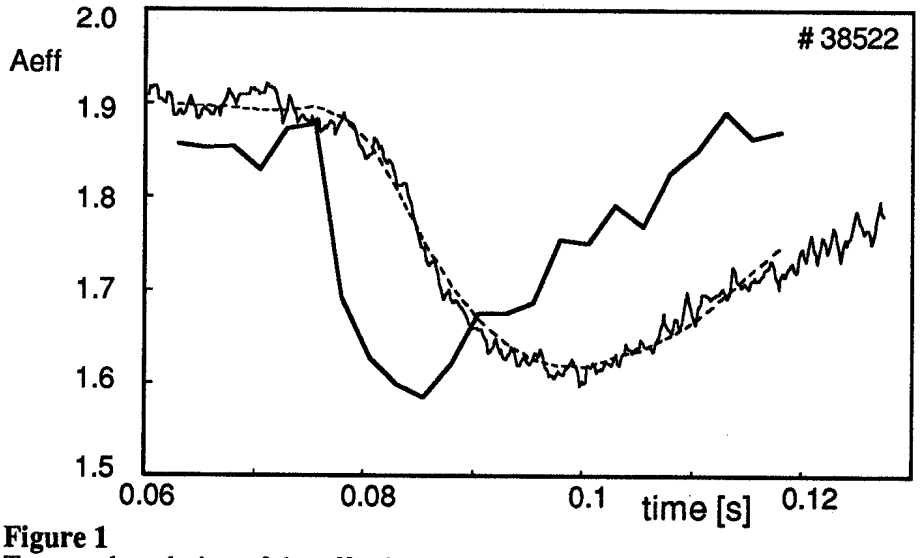

Figure 1
Temporal evolution of the effective mass during hydrogen injection in a deuterium plasma, showing : R_A measured at the edge (bold line), Aeff measured at the centre (plain), Aeff as simulated from R_A (dashed) with the transfer function shown in fig. 2.

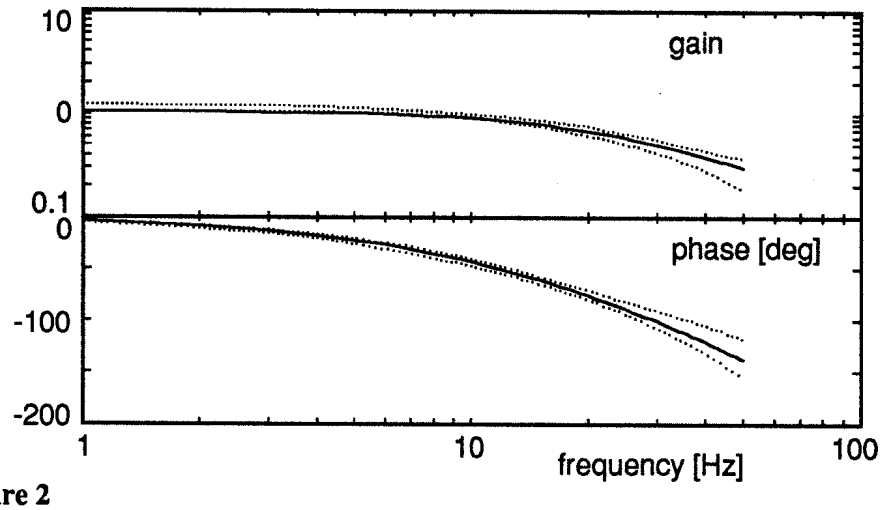

Figure 2
Bode diagrams of the transfer function as extracted from fig. 1, showing : the gain $|H(\omega)|$ and the phase $\angle H(\omega)$ with their measurement error (dotted line), the gain and the phase as calculated from the best fit for D and v (plain line).

EFFECTS OF BORONISATION ON THE PLASMA PARAMETERS IN TCA

Th. Dudok de Wit, B.P Duval, Ch. Hollenstein, B. Joye

Centre de Recherches en physique des plasmas
Association Euratom-Confédération Suisse
Ecole Polytechnique Fédérale de Lausanne
21, Av. des Bains, CH-1007 Lausanne Switzerland

INTRODUCTION Wall conditioning and deposition of low Z materials on the first wall and limiters play an important role in plasma impurity control. Carbon film deposition (carbonisation) is already used on many Tokamaks. As proposed by Veprek [1], a film containing boron and carbon would be more resistant to chemical erosion and could also getter the oxygen. This procedure (boronisation) has been tried on Textor [2], Asdex [3] and recently on TCA. The TCA vacuum vessel, the 8 rf antenna groups and 4 antenna screens are stainless steel and there are 4 carbon limiters placed in one poloidal plane.

FILM DEPOSITION AND COMPOSITION Boronisation was achieved with a four hour glow discharge at room temperature. A single antenna without rf assistance produced the discharge in a gas mixture of 80% He, 10% CH_4 and 10% B_2H_6 at a pressure of 5 10^{-3} mbar. A discharge current of 1 A was maintained by an antenna voltage of 400 V (current density 10 $\mu A/cm^2$). A film thickness between 30 and 70 nm [4] was determined from surface analysis of germanium and silicon samples exposed to the boronisation glow. The boron concentration in the film was twice the value of carbon, as in the working gas. A high oxygen concentration (18%) was measured, which was not observed to enter the plasma during tokamak operation. In a second boronisation, the oxygen concentration in the film fell to 7%.

PLASMA PARAMETERS 1) Impurities: After boronisation, the vacuum vessel base pressure decreased, the main improvement being a reduction of 5 in the partial pressure of water and a large reduction in the partial pressures of the hydrocarbons. It should be noted that TCA was not as *clean* as has previously been obtained after several months of uninterrupted operation. Thus, the conditions before boronisation should not be considered as the best achieved on TCA. The impurity content of the tokamak plasma is illustrated by the evolution of the radiated power profile measured with a 16

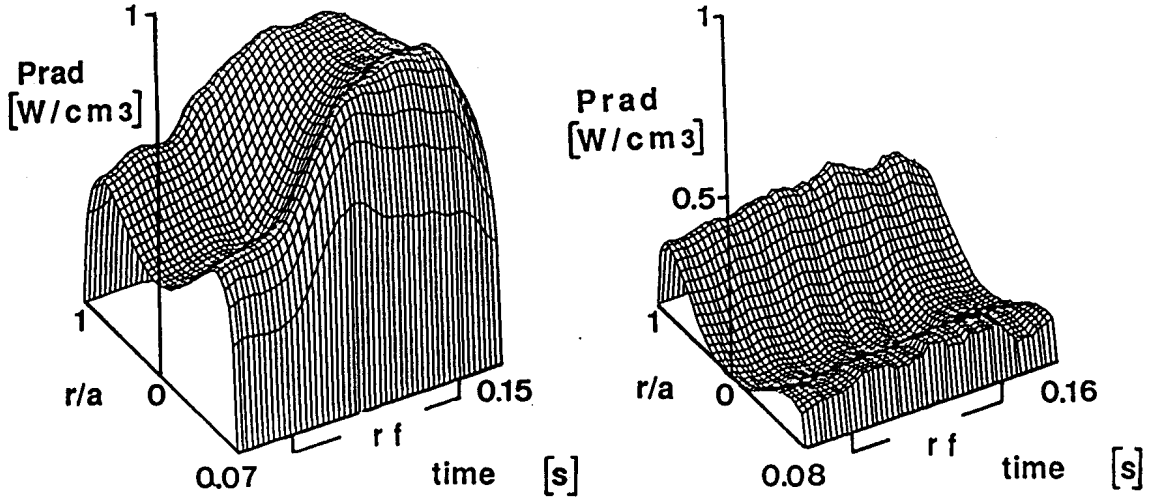

Fig 1 *Evolution of the radiated power profile before (left) and after boronisation (right)*

channel bolometer array (Fig.1). Before boronisation the profile was slightly hollow with 0.25 W/cm^3 on axis indicating that heavy impurities were present in the discharge. The increase in radiated power during the Alfvén Wave rf pulse is in part due to the increase in plasma density, but also to impurities. After boronisation, the core radiated power dropped to an unmeasurable level, indicating that the plasma was free of heavy impurities and the edge power radiation, representative of the light impurities, decreased by a factor of 4. The increase during the rf pulse is now fully explained by the electron density. The ratio of total radiated power to the input power dropped from 65-70% before boronisation to 25% after, modifying the global power balance. An increase of the electron thermal conductivity of 50% was measured from heat pulse propagation analysis during the sawteeth. Other evidence of the reduction of all impurities was the decrease of a factor of 40 of the soft X- ray fluxes measured through a 7 μm Be filter. The sawteeth inversion radius did not change, but the relative amplitude of the sawteeth and their period both increased by a factor of 2.

Spectral line analysis was performed by VUV and Visible spectrometers. The VUV observations of CIV and OVI line emission indicated a reduction of ~5 and ~20 in the impurity content normalised to plasma density (Fig 2). Spectral features from Cr I (not ionised) were observed on the outer carbon limiter, but disappeared immediately after the boronisation. We concluded that the TCA limiters were contaminated with heavy metal impurities, but that the boronisation film effectively shielded the old limiter surface from the plasma. Together with the bolometer data we conclude that the heavy metal plasma content was reduced to extremely low levels.

The improved plasma purity reduced the plasma loop voltage from 1.8 to 1.3 V resulting in an increase of the discharge current flat top of 60% (Fig 3). This figure also shows the evolution of the plasma resistance and the electron density during the rf pulse. The excellent conditions obtained with boronisation degraded slightly, and also differently for the light and heavy impurities. After ~500 discharges, with no glow discharges to clean the walls and limiters, the total radiated power increased by a

factor of two, which was well explained by increases in the light impurities (mostly carbon). The heavy impurities monitored by the soft X-ray emission and central power emission from the bolometer significantly increased. The Cr I spectral lines on the outer limiter returned to their pre-boronisation levels indicating that the limiter was no longer covered.

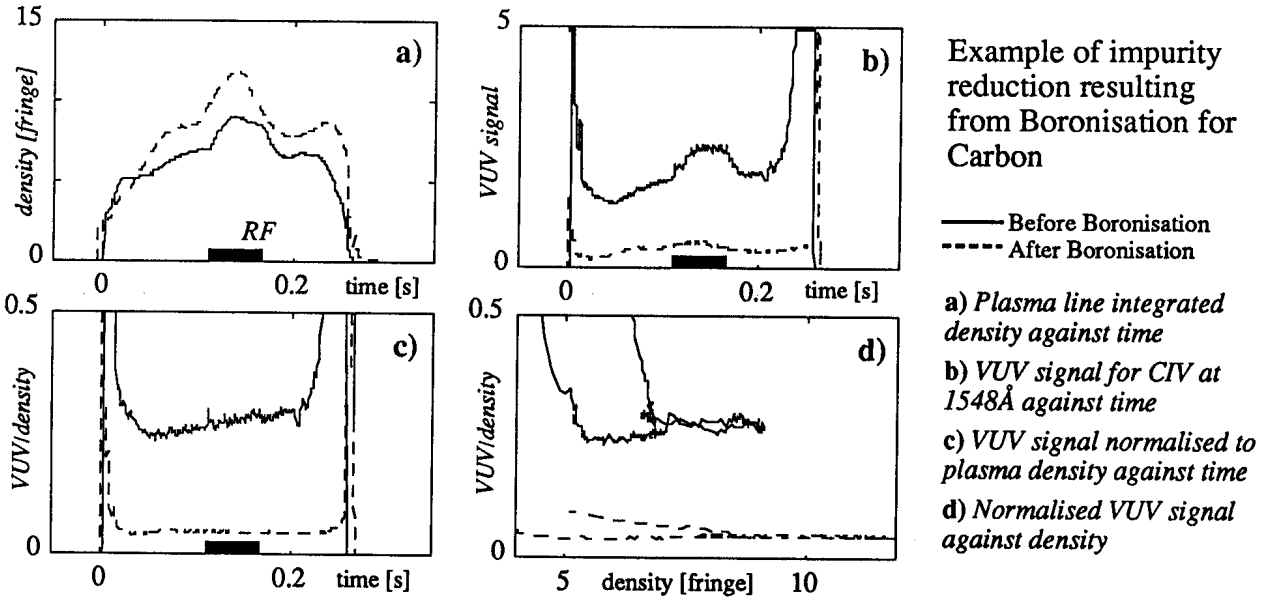

Fig 2: *From the raw traces of plasma density a) and CIV line intensity b), c) shows the CIV line intensity normalised to the plasma density through the plasma discharge. We see that the impurity increase during the RF pulse is accounted for by the increased plasma density, and that the small impurity accumulation before Boronisation is removed by Boronisation. In d) the locus of the normalised CIV line intensity is plotted against plasma density from which we deduced a reduction of ~5 in the Carbon content. A similar result was obtained with a CIII line and a reduction of ~20 from observations of OV and OVI spectral features*

Several hours of glow discharge in hydrogen restored most of the conditions following boronisation and even further reduced the carbon impurity level, although the heavy metal content was not greatly affected. Even after ~900 discharges, the plasma performance was still much better than before boronisation.

2) Density and recycling: At low to moderate densities, the plasma density control was possible except during the Alfvén Wave rf pulse where the unavoidable density increase remained a function of the rf power [5]. The recycling coefficient increased at high density impeding a rapid decrease of the plasma density. Due to the presence of hydrogen in the film, the plasma isotope mixture could not be chosen arbitrarily. Immediately after the boronisation, the ratio of D/H with a deuterium filling gas decreased through the discharge to ~1 at the end. After further discharges in deuterium, spectroscopic measurements indicated that the hydrogen concentration dropped to <5%. Extensive glow discharges in hydrogen reduced the deuterium concentration to nearly zero. This was confirmed by the measurement of the effective mass of the plasma core using the Discrete Alfvén Waves [6]. A lowest value of 1.05 was

achieved indicating that not only the deuterium concentration but also the impurity concentration were reduced to a very low level. The boronised vessel seems to hold more gas and to change working gas it is necessary to empty the stored gas using helium glows or to replace the working gas using a hydrogen or deuterium glow.

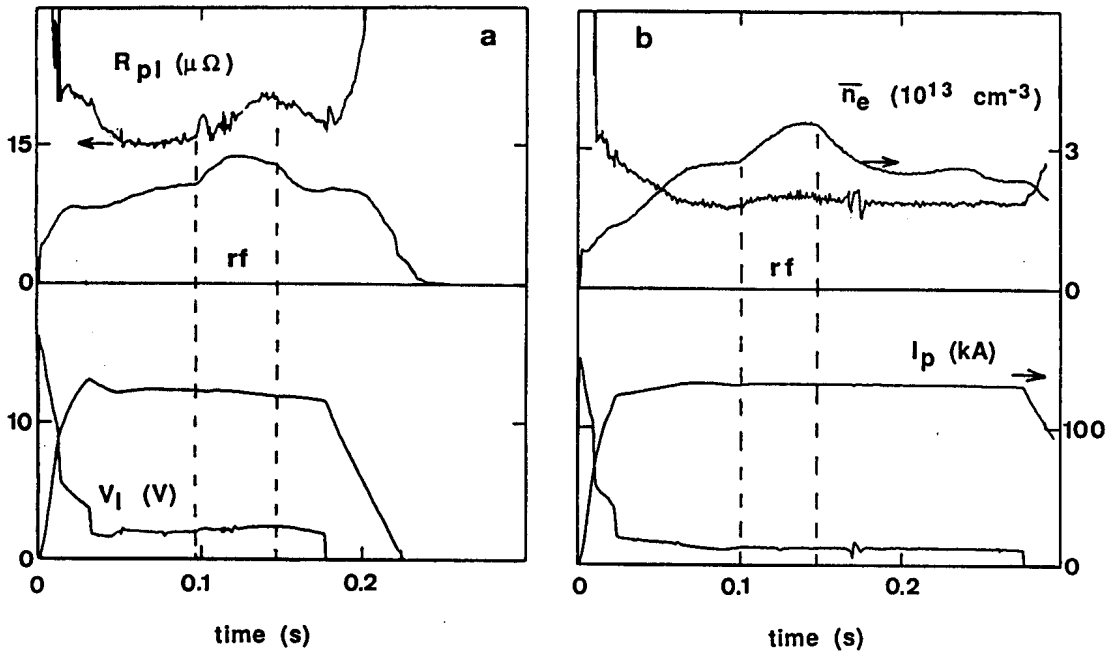

Fig 3 *Time evolution of the plasma current, loop voltage, plasma resistance and electron density: a) before, b) after boronisation*

CONCLUSION Boronisation in TCA has led to a large decrease in the level of all observed impurities (except boron !) by a factor of 5 or more. The smaller loop voltage allowed a gain of 60% of the current flap top length. Despite the high gas content in the coating, clean deuterium and hydrogen plasmas were obtained following different glow discharge cleaning. The boronisation film holds more working gas than the unboronised plasma vessel.

Acknowledgements: This work was partly funded by the Fonds National Suisse de la Recherche Scientifique.

References:

[1] Veprek S. et al. J. nucl Mater. **63** (1976) 405
[2] Waelbroeck F. et al. Plasma Physics and Controlled Fusion **31** (1989) 185
[3] Asdex team, Paper presented at the 9th Plasma Surface Interaction Conf.(1990)
[4] Hollenstein Ch. et al. ibid
[5] Collins G.A. et al. Proc. of the 12th European Conf. on Contr. Fusion and Plasma Physics, Budapest, Vol 9, p. 248 (1985)
[6] Dudok de Wit Th. et al. Particle transport studies on TCA using the dynamical response of the effective mass; presented at this conference.

ION TEMPERATURE MEASUREMENTS IN THE TCA TOKAMAK BY COLLECTIVE THOMSON SCATTERING

M. Siegrist, R. Behn, D. Dicken*, B. Duval, J. Hackmann,* B. Joye, J. Lister, C. Nieswand, A. Pochelon, G. Soumagne, D.C. Yuan

Centre de Recherches en Physique des Plasmas
Association Euratom - Confédération Suisse
Ecole Polytechnique Fédérale de Lausanne
21, Av. des Bains, CH-1007 Lausanne/Switzerland

*Institut für Laser- und Plasmaphysik, Universität Düsseldorf, West Germany

ABSTRACT

Collective Thomson scattering, using a high-power pulsed D_2O laser at 385μm and a heterodyne receiver system, has provided local ion temperature (T_i) measurements of the plasma in the TCA tokamak. Recent improvements in the noise-equivalent power (NEP) of the Schottky barrier diode mixers permitted us to achieve a typical precision of ±12% for a single shot measurement at densities above $10^{20}m^{-3}$. Even at densities of standard TCA discharges ($5x10^{19}m^{-3}$) the uncertainty is better than ±25%.

For the interpretation of the measured spectra and the evaluation of T_i the local value of the electron temperature (T_e) is an important parameter. Therefore, T_e was measured simultaneously by incoherent Thomson scattering at 0.694μm during a series of shots. The density was obtained from a far-infrared interferometer. An independent measurement of T_i on TCA can be obtained from a neutral particle analyzer (NPA). Comparison of the results from the two methods showed good agreement.

The precision of a T_i-measurement depends strongly on the plasma density. Since an uncertainty of ±25% at standard densities may still not be regarded as satisfactory, further investigations using a numerical simulation code have been carried out to find ways of improvement.

INTRODUCTION

Last year we reported the first single shot ion temperature measurements in a tokamak by collective Thomson scattering (CT) [1]. The precision was estimated to be of the order of 25%. This could not yet be considered as sufficient accuracy compared to other T_i diagnostics and hence improvements were required. On the other hand, two important questions still had to be answered: (1) are the observed spectra indeed produced by scattering from thermal velocity distributions and (2) is the ion temperature obtained from collective Thomson scattering in agreement with results from other diagnostics.

In this paper we report measurements which were undertaken to investigate these points.

APPARATUS

The experimental set-up has been described in detail in ref [1]. We will only briefly recall the main components: A CO_2 laser which delivers 600J on the 9R(22) line in a 1.4μs long single mode pulse is used for optical pumping of a 4m long unstable resonator containing 6.5mbar of D_2O vapor. The far infrared laser produces 0.5J during 1.4μs at the wavelength of 385μm.

The D_2O laser emission is focused to a 3mm waist close to the plasma center via a set of off-axis parabolic mirrors. The scattered light is collected at 90° to the incident beam in a solid angle of 4.3×10^{-3} sr.

For detection and spectral analysis of the scattered radiation we use a heterodyne receiver with an optically pumped CD_3Cl laser as local oscillator. Its emission is combined with the scattered radiation in an optical diplexer and mixed in a Schottky barrier diode. The resulting IF signal around 3.6 GHz, is amplified and split into twelve channels with a bandwidth of 80 MHz each. Thereafter the signals are integrated and digitized.

A considerable improvement of the sensitivity of our detection system has been achieved through a collaboration with groups at the University of Düsseldorf and the MPI für Radioastronomie, Bonn, which provided the mixer. The double sideband system noise temperature T_{sys}^{DSB} has been measured as a function of the IF frequency. For the diode used for the measurements reported here 5000°K, corresponding to a NEP (noise-equivalent-power) of 1.4×10^{-19}W/Hz, has been obtained in the most sensitive channel.

For the interpretation of spectra obtained from collective Thomson scattering, the electron density and temperature are required. These were measured simultaneously by a far-infrared interferometer and by ruby laser scattering, respectively. An independent measurement of T_i on TCA can be obtained from a neutral particle analyzer with five energy channels with an accuracy of the order of 5%.

MEASUREMENTS

So far we have analyzed collective scattering data from several hundred plasma discharges. The observed spectra could all be interpreted assuming thermal density fluctuations taking into account the influence of impurity ions and the magnetic field. There is no indication that non-thermal fluctuations contribute to the spectrum in the parameter range of interest ($\Delta k = 230$ cm^{-1}, $\Delta\omega > 3 \times 10^9$ s^{-1}).

Table I shows the results of 8 plasma shots with fairly reproducible plasma parameters. The diagnostic systems for n_e, T_e and the NPA were all operational. It is immediately obvious that while n_e, T_e and T_i^{NPA} are very similar, thus proving that the plasmas were indeed reproducible, T_i^{CT} shows large fluctuations. This indicates that the signal-to-noise ratio was not as good as was usually the case for this particular series.

For the centermost channel (400MHz from line center) we show in table I the ratio of the scattered signal S to the standard deviation of acquisitions in the absence of a signal $\sigma(N)$, as obtained from 18 acquisitions immediately before and after the laser pulse. Simulations for the corresponding experimental conditions indicate that this ratio has to be greater than 13 in order to achieve an accuracy of better than 30% in T_i. There is a reasonable correlation between the difference $\Delta T_i = T_i^{CT} - T_i^{NPA}$ and the ratio $S/\sigma(N)$.

The last column in table I shows the FIR laser energy in arbitrary units. While the least accurate T_i measurement was obtained at the lowest laser energy, a high laser energy does not necessarily

guarantee good precision. We suspect that the mechanical stability of optical components is partly responsible for shot-to-shot fluctuations of the signal.

Based on the assumption that the plasma conditions for the 8 shots were reproducible, we averaged the measured signals in all channels. Fig 1 shows the resulting spectrum with the standard deviation from the averaging process. The spectrum is now quite smooth and can be fitted with a calculated spectrum based on the measured average plasma parameters (n_e = 1.2 x 10^{20} m^{-3}, T_e = 415 eV, z_{eff} = 2.5 (estimate)). The resulting ion temperature is 305 eV which is in excellent agreement with the average ion temperature measured by the NPA for these 8 shots: 310 eV.

In Fig 2 we present the results from an individual shot. The shaded area is $\sigma(N)$, the points are the measured signals and the curve is the fit with T_i = 280 eV. For the ratio of $S/\sigma(N) \approx 14$ at 400 MHz we expect an accuracy of ≈ 28% from simulation results. The deviation from T_i^{NPA} is less than this value.

Fig 3 finally shows the expected accuracy of an ion temperature measurement for standard TCA plasmas and the parameters of our collective Thomson scattering system, as obtained from simulation results. In this case, the frequency range covers the region from 640 to 1520 MHz which allows a more accurate determination of T_i by fitting and represents only a minor modification of the filter bank used in the current set-up.

CONCLUSIONS

Collective Thomson scattering of far-infrared radiation is a powerful tool for the determination of T_i in a tokamak. The measurements with excellent temporal and spatial resolution are based on a direct method and are in good agreement with T_i measurements obtained with other methods. The accuracy is density dependent and approaches 10% for densities around 10^{14} m^{-3}. Further improvements are still possible, e.g. by using cooled Schottky diodes.

TABLE I

The measured plasma parameters of 8 reproducible TCA plasma discharges

shot #	n_e ($*10^{13}cm^{-3}$)	T_e (eV)	T_i^{NPA} (eV)	T_i^{CT} (eV)	$\lvert\Delta T_i\rvert/T_i^N$ (%)	$S/\sigma(N)$ (@400MHz)	E_L (AU)
37720	12.2	450	310	260	16	6	60
37721	11.7	450	320	290	9	9	80
37722	12.2	400	315	370	17	16	70
37725	12.2	450	310	220	29	13	85
37726	11.9	420	300	160	47	5	55
37727	11.9	450	310	280	10	9	90
37728	11.8	380	300	180	40	3	105
37730	11.3	330	330	300	9	14	105
averaged spectrum	12.0	415	310	305			
average of indiv. shots	12	415	310	260	22	9	80

REFERENCES

1. Behn R. et al., Physical Review Letters 62, (1989) 2833-36.

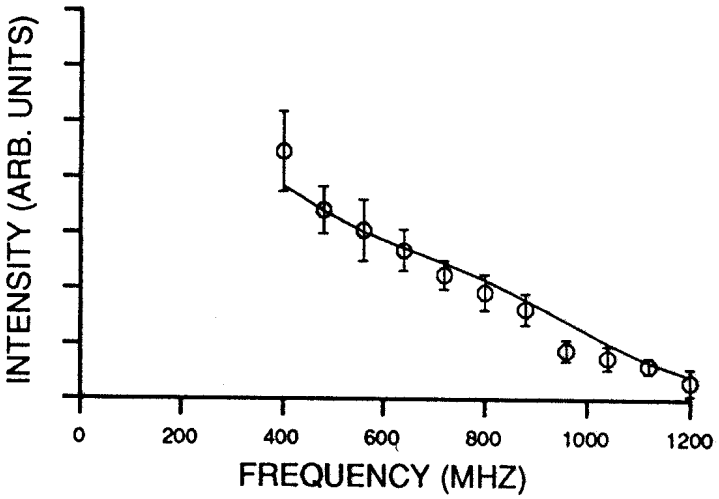

Fig. 1: The average and standard deviation of 8 measured spectra obtained from reproducible plasma discharges. The plasma parameters correspond to table I. The solid line is a least square fit, yielding $T_i = 305$ eV.

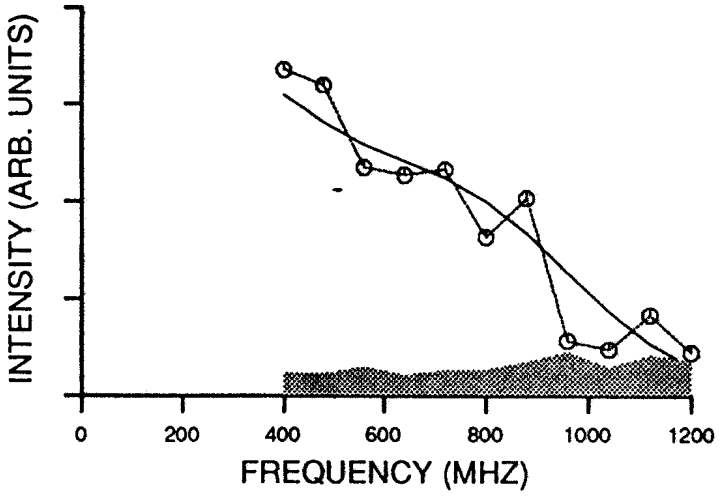

Fig. 2: Fit to an individual spectrum with time resolution of 1.4μs. The shaded region is $\sigma(N)$ (see text). Measured plasma parameters: $n_e = 7.2 \times 10^{19}$ m^{-3}, $T_e = 500$ eV, $T_i^{NPA} = 320$ eV, $z_{eff} = 2.5$. The fit (solid line) yields $T_i^{CT} = 280$ eV.

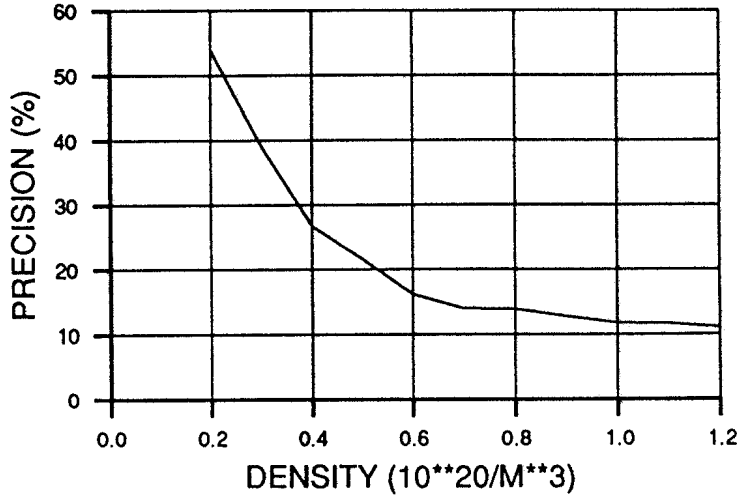

Fig. 3: The accuracy of an ion temperature measurement in D as function of plasma density for $T_e = 700$ eV, $T_i = 400$ eV and $z_{eff} = 2.5$, for 12 optimally placed frequency channels of 80 MHz width. The scattering angle is 90° and the laser frequency 780 GHz. (Simulation results).

Transition to High Density Discharges through Hard Gas Puffing

Ch.Nieswand, Z.A. Pietrzyk, A. Pochelon, R. Behn, A. Knight.

Centre de Recherches en Physique des Plasmas
Association Euratom-Confédération Suisse
Ecole Polytechnique Fédérale de Lausanne
21 av. des Bains, CH-1007 Lausanne Switzerland

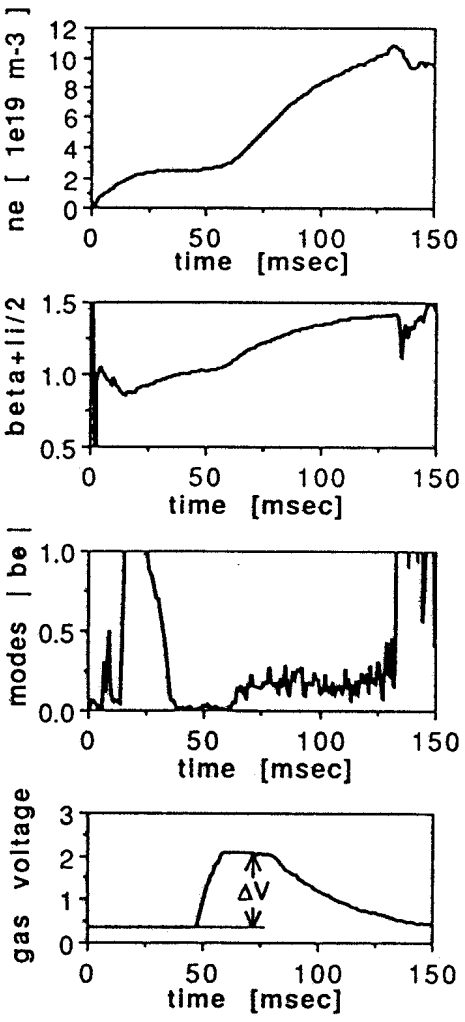

Fig. 1. Time evolution of line density, b_p+l_i/2, mode activity and gas valve voltage.

For certain experiments, and to improve plasma performance, high values of plasma density are required. The density limit for quasi stationary discharges (QSD), with soft gas puffing, is approximately $5 \cdot 10^{19}$ m^{-3} in the TCA tokamak. We have observed, however, that higher line average densities, above 10^{20} m^{-3}, can be obtained by hard gas puffing. When this hard puffing is followed by a gentle decrease of the gas flux, reproducible discharges without disruption can be obtained. In these discharges the density limit achieved $\bar{n}_e R/B_t = 3.9 \cdot 10^{19}$ $m^{-2}T^{-1}$ (for $q_a = 3.2$), was similar to that found in a similar sized machine[1] and to that observed in JET[2]. The Troyon β_{tor} limit[3], which for TCA at $q_a = 3.2$, is 1.3%, was closely approached at the end of these discharges near the density limit. All of the data to be presented were obtained on TCA with boronized walls at constant plasma current and with $q_a = 3.2 \pm 0.1$, although it is believed that the main features do not depend on the treatment of the walls.

A Thomson scattering system was used to measure the electron temperature and density at ten radial points and a single time in the discharge. Other standard TCA diagnostics were also used. Figure 1 shows the typical time dependence of the gas valve voltage,

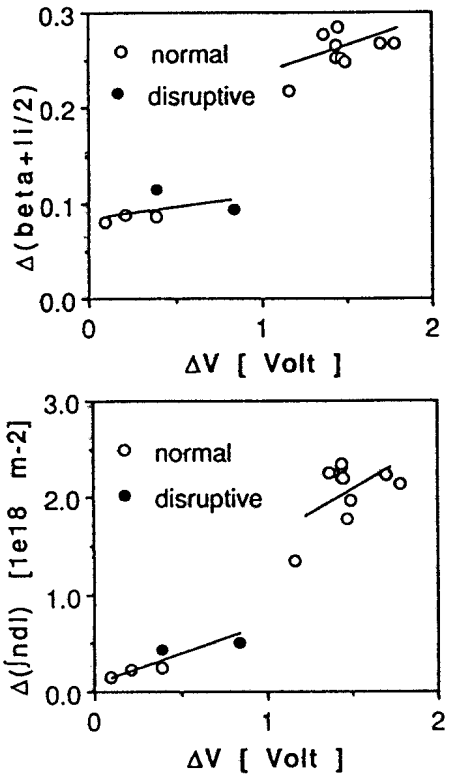

Fig. 2. Change in line density and $b_p+l_i/2$, as a function of gas step voltage.

together with the electron density, $\beta_p+l_i/2$ and the level of mode activity. In these hard puffing discharges the plasma density and $\beta_p+l_i/2$ responded in a highly non-linear fashion to the gas input. Figure 2 shows the change in density and $\beta_p+l_i/2$, defined as the difference between their values at the beginning of the hard puff and 40 ms later, as a function of the height of the gas valve voltage pulse. For low gas valve voltages, the plasma density increased until the typical QSD density limit was reached, whereupon large mode activity generally led to a disruption. As the voltage was increased further, there came a point when the plasma gas acceptance suddenly increased and the plasma attained a much higher density. By this hard puff method, strong mode activity and disruptions at the QSD density limit could be avoided. A similar discontinuity in the behaviour of $\beta_p+l_i/2$ was also observed. The hard puff produced only a moderate increase in mode activity and an increase in the plasma resistance at later times. These observations are indicative of a transition to a different discharge regime.

The response of other plasma parameters to the hard puff is shown in Figs. 1 and 3. In general, the plasma started to react to the puff after a delay of about 5 ms. At this time the parameters $\beta_p+l_i/2$, T_e, $\bar{n}_e$ and T_i (not shown in these figures) started to increase. In addition, the density profile flattened ($n_e(0)/\langle n_e\rangle$ decreased) and the temperature profile peaked. Initially the electron temperature increased for about 20-25 ms which is 3 to 9 times longer than the energy confinement time τ_E = 4-7 ms at this time. Within experimental error the increase in $\beta_p+l_i/2$ can be attributed solely to the increase in β_p, however the fact that the temperature peaking ($T_e(0)/\langle T_e\rangle$) increased suggests that l_i may also have increased. During the initial phase the sawtooth period increased linearly with the density (Fig. 4), in approximate agreement with the TFR sawtooth scaling.[4] The change in mode activity (Fig. 1) is a further indication of a change of the current profile during this initial phase.

After the initial phase the electron temperature and the peaking of the electron temperature started to decrease. The electron density began to peak at about 50 ms after the start of the puff, when the gas valve voltage was reduced, but it was always flatter than at the beginning of the discharge. $\beta_p + l_i/2$ increased continuously and β_p and β_{tor} were almost linear functions of the density up to the hard puff density limit. Measurements of the pressure profile showed that the radius of the maximum value of $|dp/dr|$ moved out for the first 50 ms of the puff. During the initial phase the sawtooth period increased linearly until the QSD density limit was reached. Thereafter it remained constant and only started to increase again near the density limit for these hard puff discharges (see Fig. 4).

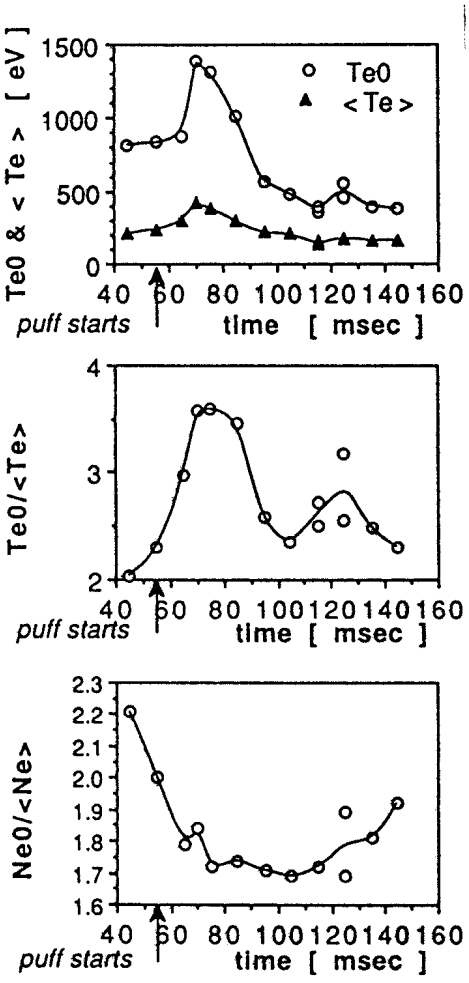

Fig. 3. Measurements of central temperature, volume averaged temperature and temperature and density peaking factors as a function of time.

A possible explanation of the plasma behaviour at the beginning of the puff is that a large amount of cold gas reduced the temperature at the plasma edge. (This was not measured as the last exterior Thomson scattering channel was not reliable at these low densities.) As the total current remains constant, the current density on axis would increase, which would result in stronger heating near the axis and a corresponding increase in the electron temperature. It is also possible, however, that a dense cold gas blanket reduces the losses and increases the energy confinement. The ion temperature (measured by charge exchange and collective Thomson scattering[5]) increased. This is to be expected since both the electron temperature and density increased, which favours transfer of power to the ions. However, the ion temperature did not decrease at later times. The strong influx of gas at the plasma edge made the density and dp/dr profiles broader. This broadening is known to increase MHD stability against kinks.[6] Detailed numerical simulations would be needed to determine if this is why higher densities can be obtained with hard puffing. The

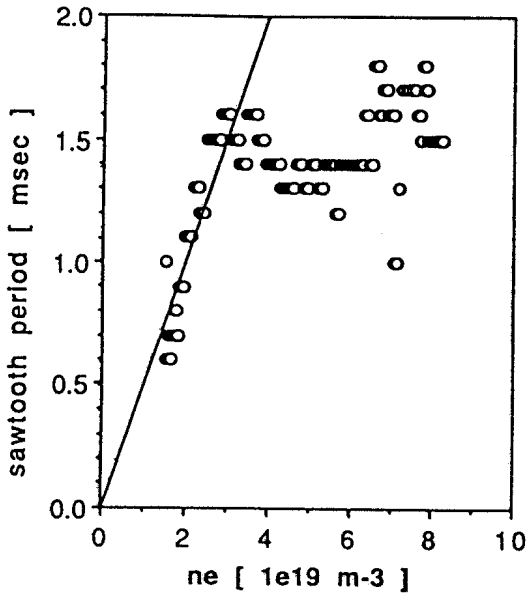

Fig. 4. Sawtooth period as a function of line averaged density for a hard puff discharge.

almost constant sawtooth period above the stationary density limit (QSDL), departing from the linear increase below the QSDL, suggests a strong modification of the current density profile. The peaking of the density profile at later times suggests that these hard puffing discharges might be similar to the IOC discharges in ASDEX.[7] However, the kinetic energy confinement time saturates at high density, as in the SOC regime.[7] Also, the ratio τ_E/n_e increased for a short time after puffing but then decreased during the later reduction of the gas valve voltage. The peaking of the density did not produce an increase in τ_E, as would be expected in an IOC discharge. The density peaking, $n_e(0)/\langle n_e \rangle$, is lower in the hard puff discharges than in QSDs near the QSD density limit. We conclude that these hard puffing discharges are not IOC discharges. Nevertheless, the method of hard puffing reported here allows plasmas to be created which are close to the Murakami density limit and the Troyon β limit.

The authors acknowledge stimulating discussions with Dr. A. Bondeson and Prof. F. Troyon, as well as the experimental support of the TCA group. This work was supported by the Swiss National Science Foundation.

References

1. M. Greenwald , et al., MIT report PFC/JA-86-22 (1988)
2. C. G. Lowry and JET team, APS Plasma Physics Meeting, Anaheim, USA (1989). (Also JET report JET-P(89)80)
3. F. Troyon, et al., Plasma Phys. and Contr. Fusion **26**, 209 (1984).
4. C. W. Simm, Ph.D. Thesis, Lausanne report LRP 334/87 (1987)
5. M. S. Siegrist, et al., this conference.
6. G. Schultz, et al., Lausanne report LRP 396/90 (1990)
7. F. X. Söldner, et al., 16th European Conference on Controlled Fusion and Plasma Physics, Venice, part I, 187 (1989)

ION CYCLOTRON WAVE EXCITATION BY DOUBLE RESONANCE PARAMETRIC COUPLING

A. Fasoli, T.N. Good, P.J. Paris, F. Skiff+, M. Q. Tran

Centre de Recherches en Physique des Plasmas
Association Euratom - Confédération Suisse
Ecole Polytechnique Fédérale de Lausanne
21, Av. des Bains - CH-1007 Lausanne - Switzerland

Introduction.

The term Double Resonance indicates generally a non-linear coupling between an electron plasma resonance (in our case, the Upper Hybrid,UH) and a low frequency eigenmode (typically, in a magnetized plasma, the ion cyclotron mode) [1]. The modulated parametric decay has been investigated in the past, both in theory [2] and in experiments [3], mostly in the context of plasma heating, in order to decrease the power threshold required in the case of a monochromatic pump wave. More recently, renewed interest has been shown in connection with experiments on large scale modification of the ionosphere [4].

In the experiment reported herein, we studied the modulated UH resonance as an *internal* antenna for Electrostatic Ion Cyclotron (EIC) waves. A method for a selective excitation of the Bernstein mode, based on the choice of the modulation excursion, is proposed.

1.Experimental set-up and diagnostic apparatus.

The experiment has been performed on the Linear Magnetized Plasma (LMP) Q-machine [5]. The plasma column has a length of about 470 cm and a diameter of 5 cm. The axial B-field is of the order of 0.3 T ($f_{ce}\approx 8$ GHz, $f_{ci}\approx 30$ kHz). Densities are of the order of 10^9-10^{10} cm^{-3}; $T_e \equiv T_{i\perp} \equiv 2T_{i\parallel} \equiv 0.2$eV. Sheath acceleration at the hot plate causes a supersonic ion drift $v_D \equiv 1.2\times10^5$ cm/s.

The RF launching system is composed of a high frequency (7-12 GHz) generator, a Traveling Wave Tube amplifier (20W), and an open waveguide disposed in the extraordinary mode inside the vacuum chamber and facing the plasma at a distance of about one cm. The maximum power flux to the plasma is of the order of 1 W/cm^2. A lay-out of the LMP device, with the geometry of the launching and detection systems, is shown in fig.1.

The diagnostic apparatus, mainly devoted to the study of the ion features, is based on the technique of Laser Induced Fluorescence (LIF) [6]. Direct information on the ion distribution function and the related moments (density, ion temperature, drift velocity, etc.) can be obtained. In the case of collisional pumping of the quantum states, a measurement of the line intensity ratio for two different transitions enables one to infer the electron temperature.

2.The monochromatic wave.

We considered an electromagnetic (e.m.) wave in the UH frequency regime: $f_{UH}(r) \equiv (f_{ce}^2 + f_{pe}^2(r))^{1/2}$ ($\approx f_{ce}$). When the e.m. wave propagating in the X-mode across the density profile encounters the UH resonance, its E-

field enhances in amplitude and tends to become parallel to the wave vector. An efficient conversion to the electrostatic Electron Bernstein Wave (EBW) can then take place. Radial probe measurements confirmed the presence of these e.s. oscillations ($k_\perp \rho_e^{exp} \cong 2\times10^{-3}$). Strong local electron heating is produced by the enhanced field at resonance.

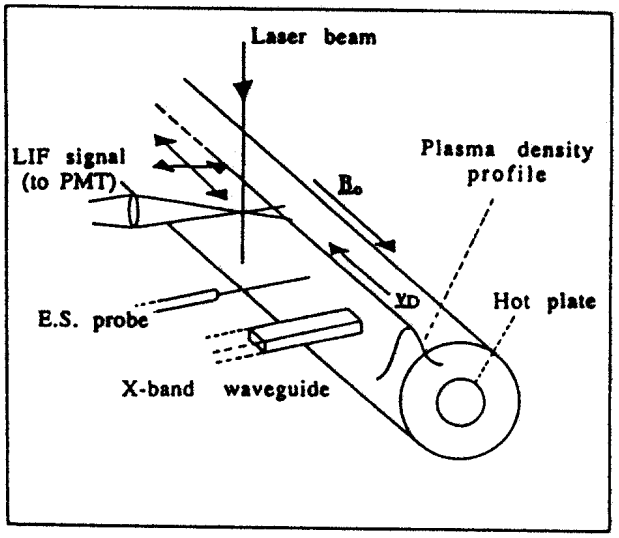

Fig.1:LMP experimental set-up

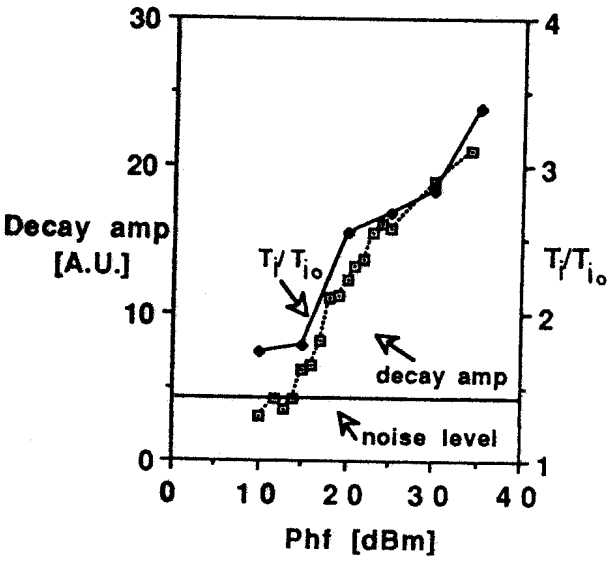

Fig.2:Decay amplitude and ion heating effects vs. RF pump power at resonance (r/a=0).

Along with the linear conversion, non linear parametric effects occur. When the driving wave is kept at resonance, a signal around f_{ci} and its harmonics is seen on the low frequency fluctuation spectrum. By scaling the frequency of this signal with the B-field ($f^{decay} \approx (1+\delta)\times f_{ci}$, with $\delta=0.2$), and by measuring perpendicular and parallel wavenumbers, we identified the decay product to belong to the forward branch of the EICW dispersion relation. Ion heating has been observed in correspondence to the parametric decay; the decay amplitude and the increase in T_i are represented as a function of the RF power in fig.2. A relatively low level for the instability threshold, buried into the background noise, has to be noticed.

3.Ion wave excitation by modulation of the h.f. resonance.

The central part of our experiment was the study of the effects of the modulation of the h.f. field, primarily in relation to the possible excitation of ion oscillations over an extended frequency domain.

When the e.m. wave is frequency modulated (f^{FM}) in the f_{ci} range, an enhancement in the level of the low frequency oscillation (≈+15 dB) with respect to the monochromatic case is observed for different pump powers. A reduction in the instability threshold can be inferred indirectly.

A first indication of ion wave propagation can be obtained from the probe signal locked to the FM driver. This signal, reported in fig.3a as a function of f^{FM}, shows, along with low frequency (drift or "edge") modes around 10 kHZ, a clear response over an entire portion of the first ion cyclotron harmonic band. To prove that this signal derives effectively from the h.f. resonance, we fixed $f^{FM}=1.2f_{ci}$ and swept the pump frequency. The

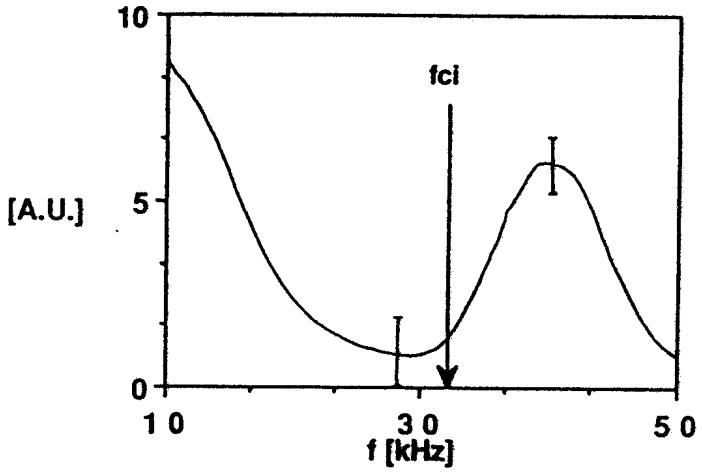

Fig.3a

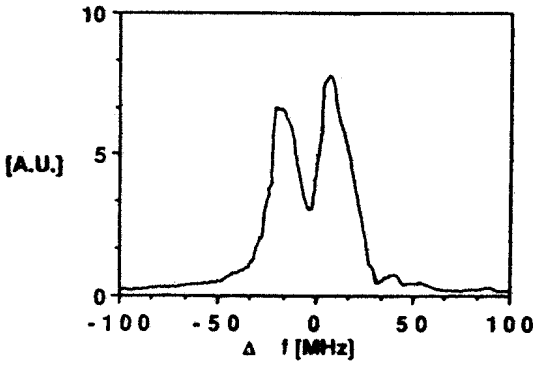

Fig.3b

Fig.3:Probe response locked to the FM driving signal: a) vs. the modulation frequency, for pump wave at resonance (≈1 W; r/a=-0.5). b) vs. the h.f. resonance detuning (Δf), for $f^{FM}=1.2f_{ci}$.

Fig.4:Perturbed perp ion distribution function; $f^{FM}=1.3f_{ci}$, P≅0.3W at resonance, r/a=-0.5, mod. excursion≅15 MHz.

Fig.5:Dependence of the measured λ on the modulation excursion (translated into the radial oscillation of the resonant layer); $f^{FM}=1.1f_{ci}$, P≅0.3W, r/a=-0.5.

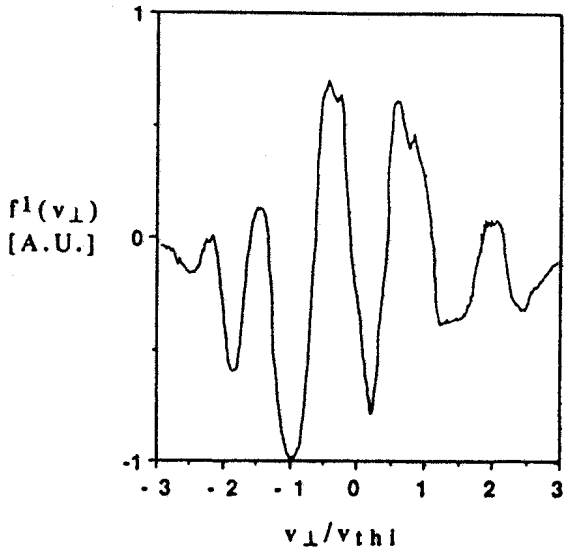

Fig.4

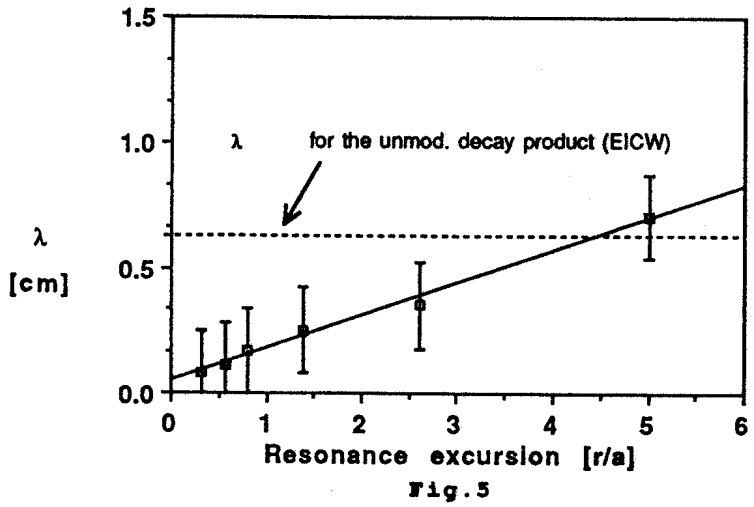

Fig.5

result is displayed in fig.3b; the signal at f^{FM} is present only for resonant pump frequencies ($\Delta f \equiv f_{UH} - f_{ce} \approx 50$ MHz).

The ion wave characteristics are investigated via LIF. The macroscopic interferograms at different modulation frequencies reveal the presence of both the forward and the backward (or Ion Bernstein, IB) branches in the EIC range. The two modes have comparable amplitudes, for the maximum modulation excursion, in contrast to the usual case of capacitive-antenna excited ion waves, where the coupling efficiency for the IBW is much smaller than for the fast mode [7]. On a kinetic level, the clearest signature of an ion wave propagating in a plasma is the presence of a perturbed ion distribution $f^1(v_\perp, v_{||})$. In fig.4 we show a typical measurement of $f^1(v_\perp)$, for an IBW driven at $f^{FM}=1.3f_{ci}$. Ballistic and free-streaming effects, which characterize the plasma perturbation induced by antennas in contact with the plasma [8], are not observable in this case. The excitation seems to occur only through collective field interaction.

Another important feature of this launching scheme, concerning the character of the excited e.s. waves, is suggested by simple theoretical considerations. In the Vlasov equation for ions, a source term can be introduced in the form of a pressure-gradient driven electric field. The pressure perturbation can be represented as $p_1(r,t)=p_1\delta(r-r_0+\Delta\cos\omega_2 t)$, where r_0 is the resonance location, ω_2 the modulation frequency (FM), and Δ the radial excursion of the resonant layer; $\Delta \equiv [d\omega_{UH}(r)/dr]^{-1} \times \omega_1$ (ω_1 is the modulation excursion). The Fourier analysis of such a field term will give a series like $\Sigma_n J_n(k_\perp\Delta)\exp(in\omega_2 t)$. The term of interest is $J_1(k_\perp\Delta)$; maximum efficiency will manifest for a fixed value of the product $k_\perp\Delta$. So, when varying Δ, the corresponding wavenumber should be determined (or "influenced") consequently. A linear dependence of $\lambda_\perp = 2\pi k_\perp^{-1}$ on the resonance excursion Δ is indeed observed in the experiment (fig.5).

Conclusions.

A localized virtual antenna for the excitation of electrostatic waves is created inside the plasma by modulating a resonant e.m. wave in the Upper Hybrid frequency regime. Wavelength and distribution function measurements identified the launched modes as EIC waves. A control on perpendicular wavelengths and a selective excitation of the IB wave can be achieved experimentally by acting on the FM modulation parameters.

***

+Permanent address: Laboratory of Plasma Research, University of Maryland, College Park, MD 20742.

The authors would like to express their gratitude to Dr.A.Wong for having inspired the experiment. This work was partly supported by the Fonds National Suisse pour la Recherche Scientifique under Grant No.20-25526.88.

References.

[1]-A.Y.Wong, D.R.Baker and N.Booth, *Phys. Rev. Lett.* **24**, 805 (1970).
[2]-D.Arnush et al., *Phys. Fluids* **16**, 2270 (1973).
[3]-K.Matsumoto and M.Sato, *Pl. Phys. and Controlled Fus.* **26**, 935 (1984).
[4]-A.Y.Wong et al., *Phys. Rev. Lett.* **63**, 271 (1989).
[5]-M.Q.Tran et al., *CRPP Laboratory Report* No. LRP 205/82 (1982).
[6]-R.A.Stern, D.N.Hill and N.Rynn, *Phys. Rev. Lett.* **37**, 833 (1981).
[7]-J.Goree, M.Ono and K.L.Wong, *Phys. Fluids* **28**, 2845 (1987).
[8]-T.N.Good et al., *this conference*.

ION WAVE EXCITATION FOR THE STUDY OF WAVE-INDUCED TRANSPORT

T.N. Good, A. Fasoli, F. Skiff*, F. Anderegg**, P.J. Paris, M.Q. Tran, N. Rynn+, R.A. Stern++ and M. Yamada+++

Centre de Recherches en Physique des Plasmas
Association Euratom - Confédération Suisse
Ecole Polytechnique Fédérale de Lausanne
21, Av. des Bains - CH-1007 Lausanne - Switzerland

Introduction

A general program to study wave-particle interactions and wave-induced transport in a low temperature, low density, collisionless plasma has led to the application of an assortment of ion wave launching schemes. These wave launching techniques include the use of : capacitively coupled rings at the plasma periphery, inductive coils, grids immersed in the plasma, and ion wave excitation by modulation of microwaves (double resonance- see paper presented at this meeting by A. Fasoli et al.). The generated ion waves are either ion acoustic, the forward and backward (neutralized ion Bernstein) branches of electrostatic ion cyclotron, and/or ballistic modes.

Our earlier studies have addressed the ion interaction with a single monochromatic wave, such as ion acceleration by intrinsic stochasticity induced by interaction with an ion Bernstein mode [1], and ion coordinate space diffusion constrained by conservation of integrals of the motion in this deterministic system [2]. In the case of linear ion acoustic wave-particle interaction, an experimental test ion approach has yielded direct evidence of phase space orbit perturbations for ions resonant with the wave phase velocity, demonstrating on the kinetic level the essence of ion Landau damping [3, 4].

We are now turning our attention to the problem of stochastic interaction with two ion cyclotron modes. A detailed knowledge of the waves excited by the antenna will allow a selection of mode phase velocities such that the separation of wave-particle resonances can be controlled. In this way, the wave field amplitudes necessary for reaching the stochasticity threshold can be reduced, in comparison to the situation with one wave [5].

This paper reviews the wave dispersion characteristics compiled during the aforementioned wave-particle interaction studies. It will be seen that the plasma dispersion relation universally determines the wave response, quite independent of the antenna configuration.

Experimental Apparatus and Methods

The experiments have been conducted in the Linear Magnetized Plasma [6] device arranged as a 470 cm long Q-machine with variable

magnetostatic field of 0.1 - 0.3 Tesla. The 5 cm diameter barium plasma can be described by the following parameters : density : 10^9-10^{10} cm^{-3}, temperatures : $T_e \cong T_{i\perp} \cong 2T_{i\parallel} \cong 0.2$ eV, ion drift velocity $v_D/v_{th} \cong 4$, and with ion-ion collision length greater than the plasma length.

Wave features were measured optically via laser induced fluorescence (LIF), by analysis of the ion dielectric response [7, 8]. Through the use of phase-lock techniques, or spatially localized measurements of the ion velocity distribution function synchronous with the wave field, a component of the perturbed distribution is observed that oscillates coherently with the wave. Single point detection of the perturbed distribution, or spatial scanning of the velocity moments of this distribution yield measurements of wave vector and amplitude. The superb velocity, spatial, and temporal resolution ($\Delta v/v_{th} < 1\%$, $\Delta x^3 \approx 1 mm^3$, $\Delta t \cong 1\mu sec$) complement the nonperturbative nature of this diagnostic.

The electrostatic antenna consists of 1 to 4 insulated metal rings, each of length $\approx$ 5 mm, maintained in contact with the plasma edge, and with variable spacing and phasing to allow an antenna wavelength from 3 - 18 cm. The electromagnetic antenna is an inductive coil of 3 cm length and situated outside the plasma radial boundary with diameter 7 cm. The planar grid (grid spacing $\approx$ 2 mm) was kept normal to the plasma column axis and covered the plasma cross section to ensure plane wave propagation parallel to the magnetic field.

Experimental Results

The measured wave dispersion relations for propagation perpendicular and parallel to the magnetic field are summarized in Figs. 1 and 2. A composite of data points from all wave launching structures is presented to underline the primacy of the role of the plasma in determining the wave response. In Fig. 1, one can recognize the resonant feature of the wave near the cyclotron harmonic frequencies. By comparison with the theoretical dispersion relation derived for these plasma parameters (displayed with constant $k_\parallel$ for aiding identification), one identifies the fast, backward branch and slow, forward branch of the electrostatic ion cyclotron mode.

The parallel dispersion of Fig. 2 shows two readily identifiable curves. The ion acoustic mode (with theoretical prediction) propagates with phase velocity equal to the sum of the ion drift and sound speeds. The fast wave is most likely the electrostatic ion cyclotron mode, since it exhibits a cutoff of the fundamental cyclotron frequency. Note also the convergence of the two dispersion curves for large $f_{RF}/f_{ci} \approx 4.5$, where the ion cyclotron frequency is indicated in the figure. A few points showing propagation at low frequency and slower phase velocity than the ion acoustic wave remain as yet unidentified.

By observing the ion density response locally as the excitation frequency is slowly swept, a coupling efficiency curve is determined for each antenna configuration as in Fig. 3. In this case, we show the

peaked response at the ion cyclotron frequency and its first harmonic, as well as a non-zero response for nonresonant frequencies below and between these values. Our results indicate that there is an evident optimum spacing for most efficient coupling at each frequency. Still, for a given frequency, we have observed no wavelength dependence on the type of antenna or on the electrostatic antenna ring spacing.

The ions responded to grid excitation in two modes : the ion acoustic waves shown in Fig. 2, and ballistic pseudowaves. The presence of the pseudowave depended on large excitation amplitude ($eV_{grid}/T_e > 1$), and could be avoided by limitation of the fluctuating grid voltage. The spatial evolution of the total time-resolved ion velocity distribution is presented in Fig. 4, under conditions where the pseudowave response dominates. In this 3-D plot, one clearly sees the velocity space propagation characteristic of ballistic ion bursts accelerated locally at the grid.

The investigation of two wave launching has been initiated as we have evaluated the importance of wave-wave interactions on the particle dynamics. Employing two electrostatic antennas, beat waves have been observed that obey the conservation laws for matching parallel wave number and frequencies. The waves beating at the difference frequency also follow the ion acoustic dispersion relation, as seen in Fig. 2.

In the context of utilizing two antennas to reach stochasticity conditions, it is important to mention some adverse effects of large amplitude excitation. For continuous wave operation in this regime, the electrostatic antenna cuts off the plasma flow beyond it, by some mechanism not yet well understood. Ions are even reflected axially and carry a ballistic perturbation upstream, like in the case with the grid. With only partial plasma cutoff, the downstream plasma profile is modified, pinching the plasma radially, and enhancing the static radial electric field and resultant plasma rotation. In a gated RF operation, a severe transient response reduces the plasma density to zero upstream too, before a new quasi-equilibrium is restored in an ion transit time.

Conclusions

A proper theoretical investigation in support of our data would involve a two-dimensional analysis of the plasma dispersion function. As shown above, both wave numbers are changing with frequency. In contrast to standard assumptions, the parallel wavelength is not fixed by the antenna structure, and the perpendicular wavelength is not fixed (but probably influenced by) radial boundary conditions. Thus the dispersion relation must be solved simultaneously for $k_\perp$ and $k_\parallel$, with frequency as the independent variable.

The problem of plasma cutoff presents an obvious impediment to coupling from two antennas separated axially. Achieving sufficient wave amplitude for stochasticity studies will isolate the downstream antenna from the plasma. These adverse effects have motivated a search for other wave-launching schemes that minimize plasma

contact with strong local antenna electrostatic fields, such as double resonance techniques [9].

Permanent addresses:

* Laboratory of Plasma Research, U. Maryland, College Park MD 20742
** Dept. of Physics, U. California San Diego, La Jolla CA 92093
\+ Dept. of Physics, U. California Irvine, Irvine CA 92717
++ U. of Colorado, Boulder, CO 80309
+++ Plasma Physics Lab., Princeton U., Princeton NJ 08543

This work was partly supported by the Fonds National Suisse de la Recherche Scientifique under Grant No. 20-25526.88.

References

[1] F. Skiff, F. Anderegg, M.Q. Tran, Phys. Rev. Lett. **58**, 1430 (1987)
[2] F. Skiff *et al.*, Phys. Rev. Lett. **61**, 2034 (1988)
[3] A. Fasoli *et al.*, Phys. Rev. Lett. **63**, 2052 (1989)
[4] A.Y. Wong, R.W. Motley and N. D'Angelo, Phys. Rev. **133**, A436 (1964)
[5] D.F. Escande, Phys. Rep. **121**, Nos. 3 and 4 (1985)
[6] M.Q. Tran *et al.*, CRPP Laboratory Report No. LRP 205/82 (1982)
[7] F. Skiff and F. Anderegg, Phys. Rev. Lett. **59**, 896 (1987)
[8] T.N. Good *et al.*, in *Nonlinear Phenomena in Vlasov Plasmas*, edited by F. Doveil (Editions de Physique, Orsaz, 1989), p. 255
[9] A. Fasoli *et al.*, this conference

Figure captions

Fig. 1 Perpendicular dispersion relation. ES - electrostatic ring antenna with 1 to 4 separated rings, EM - electromagnetic inductive coil antenna. Upstream/downstream refers to axial position of measurement relative to the antenna position and ion flow direction. Theory curve assumes electrostatic waves.

Fig. 2 Parallel dispersion relation. The echo wave was excited by two axially separated grid antennas. The beat wave was excited by two axially separated electrostatic ring antennas. ES antenna data comprises points of varied ring spacing. Pseudowave dispersion is omitted.

Fig. 3 Ion response at a single point as the EM antenna frequency is varied. The ion density fluctuation at the excitation frequency is recorded to measure the spectrum of the antenna coupling efficiency.

Fig. 4 Spatial evolution of the ion velocity distribution, as a snapshot in time, as the LIF probe is stepped away from the grid antenna on the downstream side, with respect to the ion flow. Grid excitation amplitude, $eV_{ac}/T_e \approx 30$, at a driving frequency, f = 45 kHz.

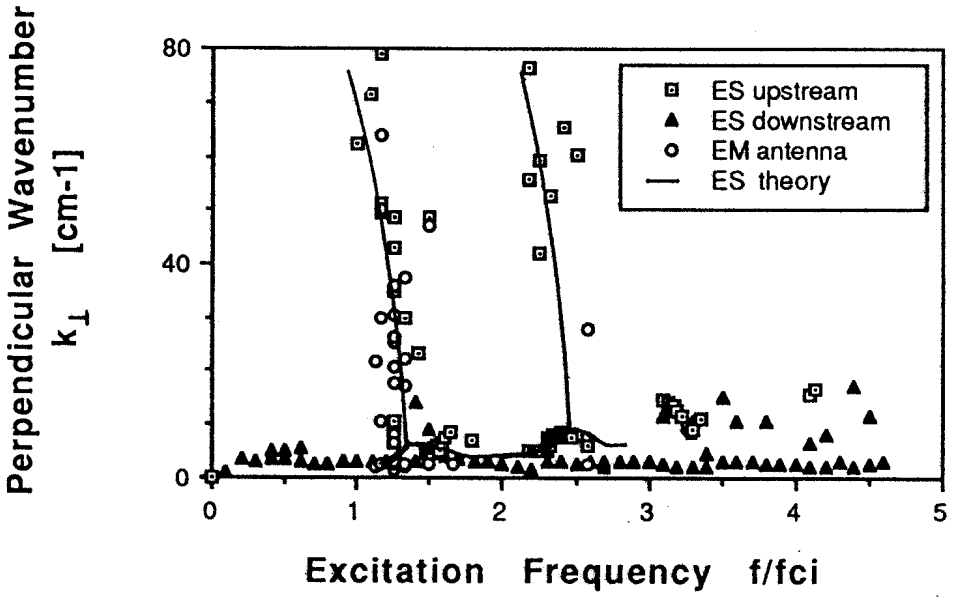
Perpendicular Wavenumber
$k_\perp$ [cm-1]
80
40
0
0
1
2
3
4
5
ES upstream
ES downstream
EM antenna
ES theory
Excitation Frequency f/fci

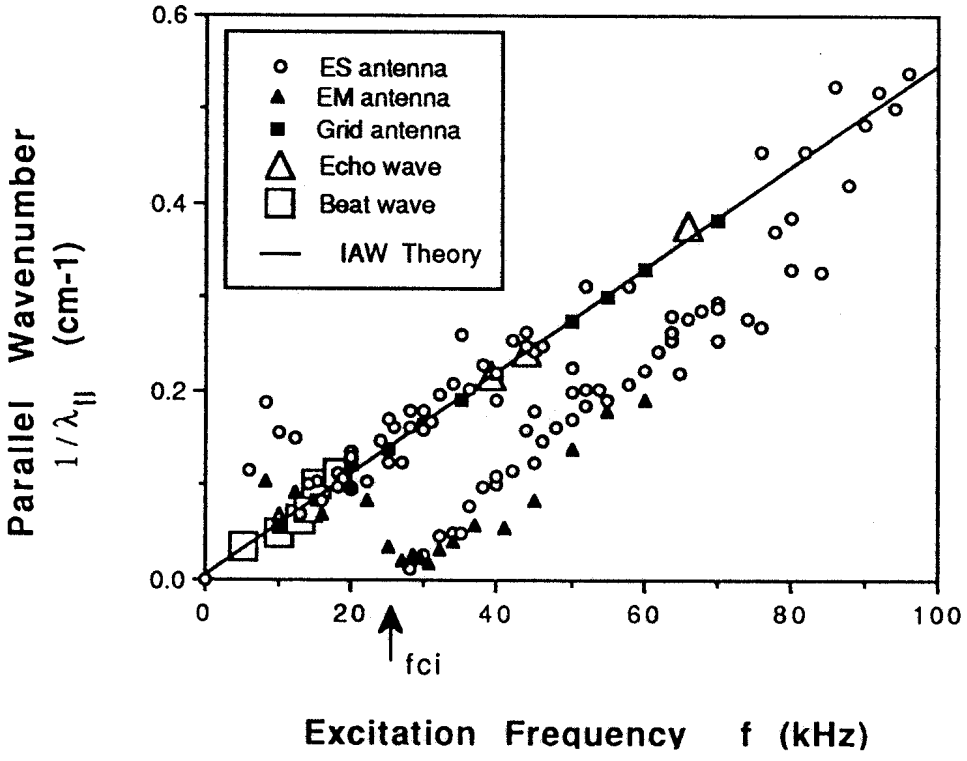
Parallel Wavenumber
$1/\lambda_{//}$ (cm-1)
0.6
0.4
0.2
0.0
0
20
40
60
80
100
fci
ES antenna
EM antenna
Grid antenna
Echo wave
Beat wave
IAW Theory
Excitation Frequency f (kHz)

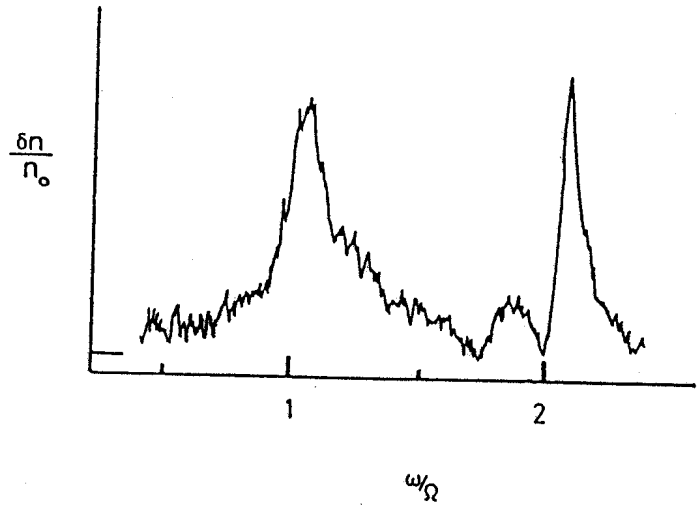
δn / n₀
1
2
ω/Ω

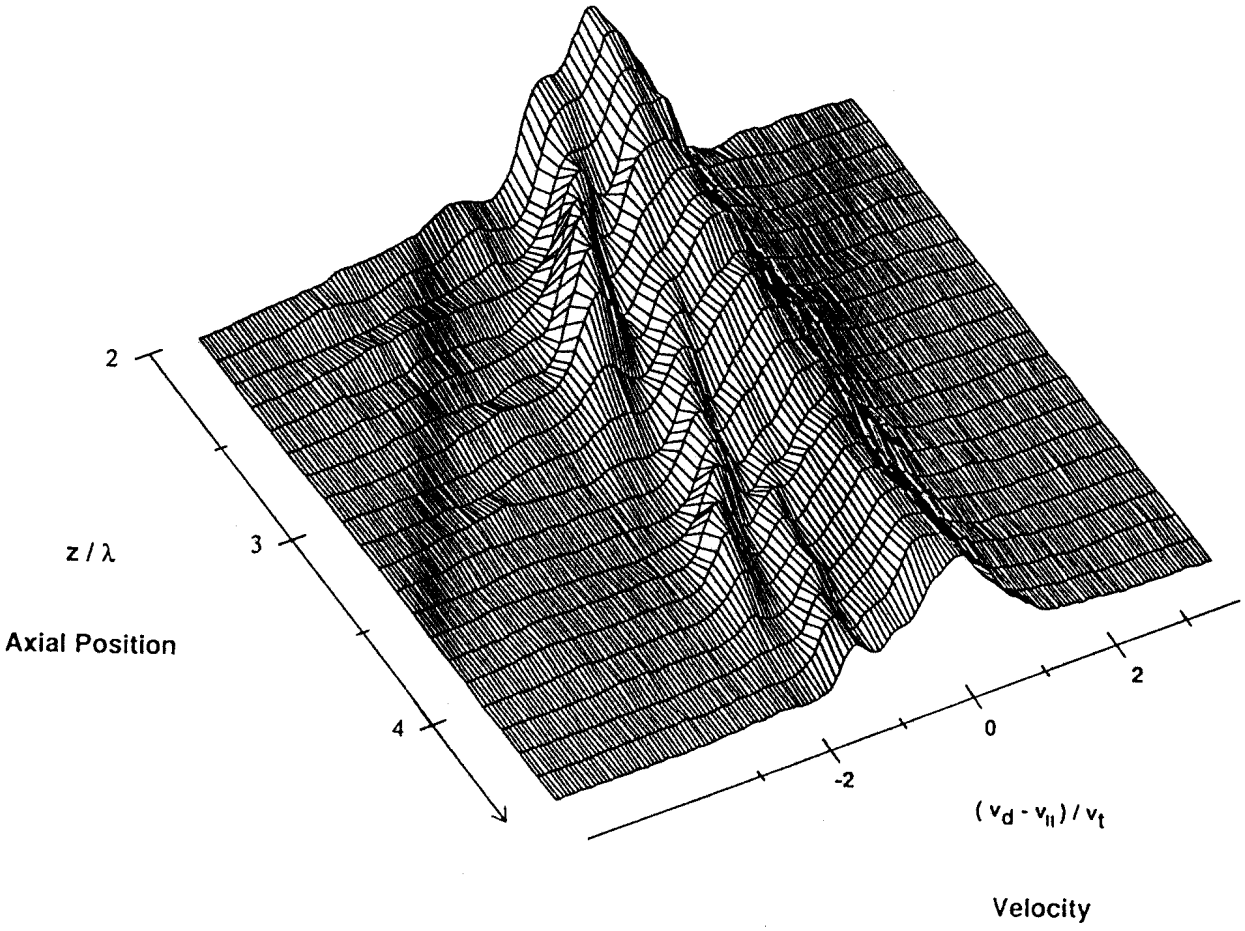
2
3
4
z / λ
Axial Position
-2
0
2
(v_d - v_∥) / v_t
Velocity